Geoderma 375 (2020) 114483

Contents lists available at ScienceDirect

Geoderma

journal homepage: www.elsevier.com/locate/geoderma

# Organo-mineral interactions and soil carbon mineralizability with variable saturation cycle frequency

Angela R. Possinger[a,1,*], Scott W. Bailey[b], Thiago M. Inagaki[c], Ingrid Kögel-Knabner[c,d], James J. Dynes[e], Zachary A. Arthur[e], Johannes Lehmann[a,d,f,*]

[a] School of Integrative Plant Science, Section of Soil and Crop Sciences, Cornell University, USA
[b] US Forest Service Northern Research Station, USA
[c] Chair of Soil Science, Technical University Munich, Germany
[d] Institute for Advanced Study, Technical University Munich, Germany
[e] Canadian Light Source, Canada
[f] Atkinson Center for a Sustainable Future, Cornell University, USA

ARTICLE INFO

Handling Editor: Yvan Capowiez

*Keywords:*
Soil organic carbon
Organo-mineral
Redox-SOC dynamics
Transient water table
Saturation cycle frequency

ABSTRACT

The response of mineral-stabilized soil organic carbon (SOC) to environmental change is a source of uncertainty in the understanding of SOC cycling. Fluctuating wet-dry cycles and associated redox changes in otherwise well-drained soils may drive mineral dissolution, organic carbon (OC) mobilization, and subsequent OC mineralization. However, the extent to which rapid fluctuations between water-saturated and unsaturated conditions (i.e., flashy conditions) result in long-term changes in mineral composition and organo-mineral interactions is not well understood. In this study, the effect of variable saturation frequency on soil mineral composition, mineral-associated OC, and OC mineralizability was tested using selective dissolution, bulk spectroscopy, microscale imaging, and aerobic-anaerobic incubation experiments. Previous water table fluctuation measurements and diagnostic profile characteristics at Hubbard Brook Experimental Forest (NH) were used to identify soils with high, medium, and low saturation frequency regimes (defined by historical water table cycling frequency; i.e., water table presence and recession in the upper B horizon). We found the amount of OC released during extractions targeting non-crystalline minerals was of similar magnitude as extracted iron (Fe) in lower saturation frequency soils. However, the magnitude of extracted OC was 2.5 times greater than Fe but more similar to extractable aluminum (Al) in higher saturation frequency soils. Bulk soil Fe was spatially more strongly correlated to soil organic matter (SOM) in lower saturation frequency soils (Spearman Rank $r_s = 0.62$, $p < 0.005$), whereas strong correlations between Al and SOM were observed in higher saturation frequency soils ($r_s = 0.88$, $p < 0.005$) using nanoscale secondary ion mass spectrometry (NanoSIMS) imaging. Characterization of bulk soil Fe with X-ray absorption spectroscopy showed 1.2-fold greater Fe(II) and 1-fold lower contribution of Fe-organic bonding in soils with high saturation frequency. Fe(III) interactions with carboxylic and aromatic C were identified with $^{13}C$ nuclear magnetic resonance (NMR) spectroscopy Fe(III) interference experiments. Additionally, carboxylic acid enrichment in high saturation frequency soils quantified by C K-edge X-ray absorption spectroscopy point towards the role of carboxylic functional groups in Al-organic in addition to Fe-organic interactions. In our incubation experiments, a doubling in short-term $CO_2$ evolution (per unit total soil C) was detected for high relative to low saturation frequency soils. Further, an order of magnitude increase in $CO_2$ evolution (per unit water-extractable OC) following anaerobic incubation was only detected in high saturation frequency soils. The observed shift towards Al-dominated SOC interactions and higher OC mineralizability highlights the need to describe C stabilization in soils with flashy wet-dry cycling separately from soils with low saturation frequency or persistent saturation.

* Corresponding authors at: 306 Tower Road, Ithaca, NY 14853, USA.
*E-mail addresses:* arp264@vt.edu (A.R. Possinger), CL273@cornell.edu (J. Lehmann).
[1] Present address: Virginia Tech, 220 Ag-Quad Ln, Blacksburg, VA, 24061, USA.

https://doi.org/10.1016/j.geoderma.2020.114483
Received 13 September 2019; Received in revised form 21 May 2020; Accepted 27 May 2020
Available online 08 June 2020
0016-7061/ 

## 1. Introduction

The accumulation and persistence of soil organic carbon (SOC) is considered to be predominantly governed by environmental variables (Schmidt et al., 2011; Lehmann and Kleber, 2015). Water saturation and associated anoxic conditions generally decrease SOC mineralization rates, leading to SOC accumulation under persistent saturation (e.g., in wetlands or flood plains) (Kayranli et al., 2010; Sutfin et al., 2016; Mayer et al., 2018). However, redox conditions in otherwise aerobic, well-drained soils can vary widely due to both spatial heterogeneity (e.g., anaerobic microsites) and flashy (i.e., rapidly fluctuating) saturation-drying cycles (Silver et al., 1999; Keiluweit et al., 2017). Reducing conditions resulting from short-term saturation events in otherwise aerobic soils may induce mineral dissolution and release SOC that was previously associated with the mineral solid phase (Buettner et al., 2014; Herndon et al., 2017; Coward et al., 2018). This relationship between water content and carbon bioavailability with frequent cycles of rapid saturation and draining is a point of uncertainty in SOC cycling, particularly in light of predicted shifts in moisture regimes with global climate change (Christensen et al., 2013).

The mechanism of mineral-SOC interaction is expected to influence the degree of susceptibility to dissolution and subsequent transformations (Winkler et al., 2018). Overall, SOC association with redox-active elements (e.g. iron, Fe, and manganese, Mn) may be more sensitive to fluctuating redox than other elements (e.g., aluminum, Al). Non- or semi-crystalline Fe phases that rapidly dissolve and re-precipitate under fluctuating redox conditions (including short-ranged order (SRO) phases, Fe-organic complexes, and Fe co-precipitated with SOC) may have increased susceptibility to dissolution under increased saturation frequency, with associated mobilization of Fe(III)-associated SOC (Buettner et al., 2014; Ginn et al., 2017; Barcellos et al., 2018; Chen et al., 2018; Chen and Thompson, 2018). However, Fe(II) may also form stable Fe(II)-organic complexes in the presence of high OC input (Bhattacharyya et al., 2018). Co-precipitation of SOC with reduced or re-oxidized Fe may also provide surface-area independent stabilization reactions (Kleber et al., 2015). For semi-crystalline minerals, Fe and Al solubilities are likely to co-vary, and Fe oxidation–reduction reactions may indirectly affect the solubility of other colloidal materials via changes in soil solution chemistry (e.g., pH) (Thompson et al., 2006a). This potential for wide variation in Fe-Al-SOC dynamics with variable saturation frequency complicates prediction of the relative role of Fe vs. Al.

With increased saturation frequency, long-term shifts in soil mineral composition and elemental ratios are likely, resulting from leaching of mobile elements, changes to mineral weathering and/or crystallization, or indirect effects on soil solution chemistry (Thompson et al., 2006a, 2011; Das et al., 2019). In particular, lower-pH soils with high Fe and Al contents may experience shifts in Fe crystallinity and elemental composition (e.g., increased Al to Fe ratio) in the long-term due to the mobilization of soluble Fe(II) with increased saturation frequency (Thompson et al., 2006b, 2011; Inagaki et al., 2020). Experimental exposure to rapid redox oscillations has also been linked to increased Fe reduction rates in Fe-rich soils (Ginn et al., 2017; Barcellos et al., 2018; Winkler et al., 2018). While Fe reduction occurs in generally aerobic soils (Yang and Liptzin, 2015; Hall et al., 2016), the effect of short-duration saturation and rapid draining events on soil mineral composition, organo-mineral interactions, and associated availability of SOC is not fully understood in upland, otherwise well-drained soils.

To test the hypothesis that higher frequency of saturated–unsaturated cycles increases the bioavailability of mineral-stabilized SOC, we used upland forest soils that span a naturally occurring gradient in mineral soil saturation cycle frequency at Hubbard Brook Experimental Forest (Woodstock, NH) (Fig. 1). Differences in saturation cycle frequency of the studied soil profiles are a result of bedrock-induced limitation on drainage (Bailey et al., 2014; Gillin et al., 2015; Gannon et al., 2017). We applied bulk soil characterization, selective extractions, and bulk spectroscopy to identify changes in reactive metal and SOC properties and organo-mineral interactions as a function of soil saturation frequency. We also related observations of soil properties to SOC mineralization potential under fluctuating anaerobic–aerobic conditions in laboratory incubations.

## 2. Materials and methods

### 2.1. Study site description

#### 2.1.1. Soil profile categorization by saturated–unsaturated cycle frequency

Soil sampling was conducted over a slope transect in Hubbard Brook Experimental Forest (Woodstock, NH) Watershed 3 (W3), a hydrological reference watershed for which a hydropedological unit (HPU) classification system was initially developed and verified (Bailey et al., 2014) (Supplementary Fig. A1). Soils in W3 are Wisconsinan glacial deposits (basal and ablation till) over Silurian Rangeley Formation bedrock (sillimanite-grade pelitic schist and calc-silicate granulite) (Gannon et al., 2017). Differences in hydrological patterns (a function of proximity to exposed bedrock and bedrock upslope contributing area) result in marked differences in soil profile characteristics, used to designate predictable soil units (Bailey et al., 2014; Gillin et al., 2015) (Fig. 1). Previous year-round water table measurements (McGuire et al., 2016) were used to estimate the frequency of water table presence and recession cycles (i.e., “saturation cycle frequency” or in brief “saturation frequency” in the rest of the paper) in the upper B horizon (usually a spodic horizon, e.g. Bhs, Bs, or Bh) for three soil units (Fig. 1). We categorized these soil units as low, medium, and high saturation frequency, with approximately 0, 3, and 5 saturation events (per 30 days) (based on McGuire et al., 2016), respectively. These categories correspond to the designation as “typical, “Bhs”, and “E” podzols used in Bailey et al. (2014), Bourgault et al. (2015, 2017), and Gannon et al. (2017) (Supplementary Fig. A1). Diagnostic profile characteristics and site physiography for typical, Bhs, and E podzols were used to determine the saturation frequency category for each soil profile (Fig. 1, Supplementary Tables A1 and A2). Similar profile characteristics associated with transient water table effects and hillslope transport are also observed in Spodosols globally (Sommer et al., 2000; Jankowski, 2014).

#### 2.1.2. Soil sampling and profile description

Locations for soil profile sampling were initially selected using predictive maps for the studied hydropedological soil units (Gannon et al., 2017) (Supplementary Fig. A1). Elevation at sampling locations spanned 603–663 m. Profile designation as E, Bhs, or typical podzols (corresponding with high, medium, and low soil saturation frequency) was conducted using in-field profile characteristics (Supplementary Fig. A1, Supplementary Tables A1 and A2). For each soil saturation frequency category, 3 profiles were sampled by pedogenic horizon (Supplementary Table A2). Profile descriptions included matrix and secondary colors, structure, horizon thickness, texture by feel, and estimated rock content (Supplementary Table A2). Horizons from surface Oi to bedrock, water table, or ~ 1-m depth were sampled quantitatively, and stored at field-moist conditions (~4°C) prior to air-drying and sieving (2 mm-mesh).

#### 2.1.3. Vegetation and organic soil layer composition

To account for potential influence of shifting dominant vegetation for the sampling sites, trees with diameter at breast height (DBH) > 0.1 m were identified to species and measured within a 310 $m^2$ sampling area (Supplementary Table A3). Across the transect, vegetation was generally mixed hardwood forest, including the deciduous tree species American beech (*Fagus grandifolia*), striped maple (*Acer pensylvanicum*), sugar maple (*A. saccharum*), yellow birch (*Betula alleghaniensis*), white birch (*B. papyrifera*), and the coniferous species balsam fir (*Abies balsamea*) and red spruce (*Picea rubens*). Vegetation

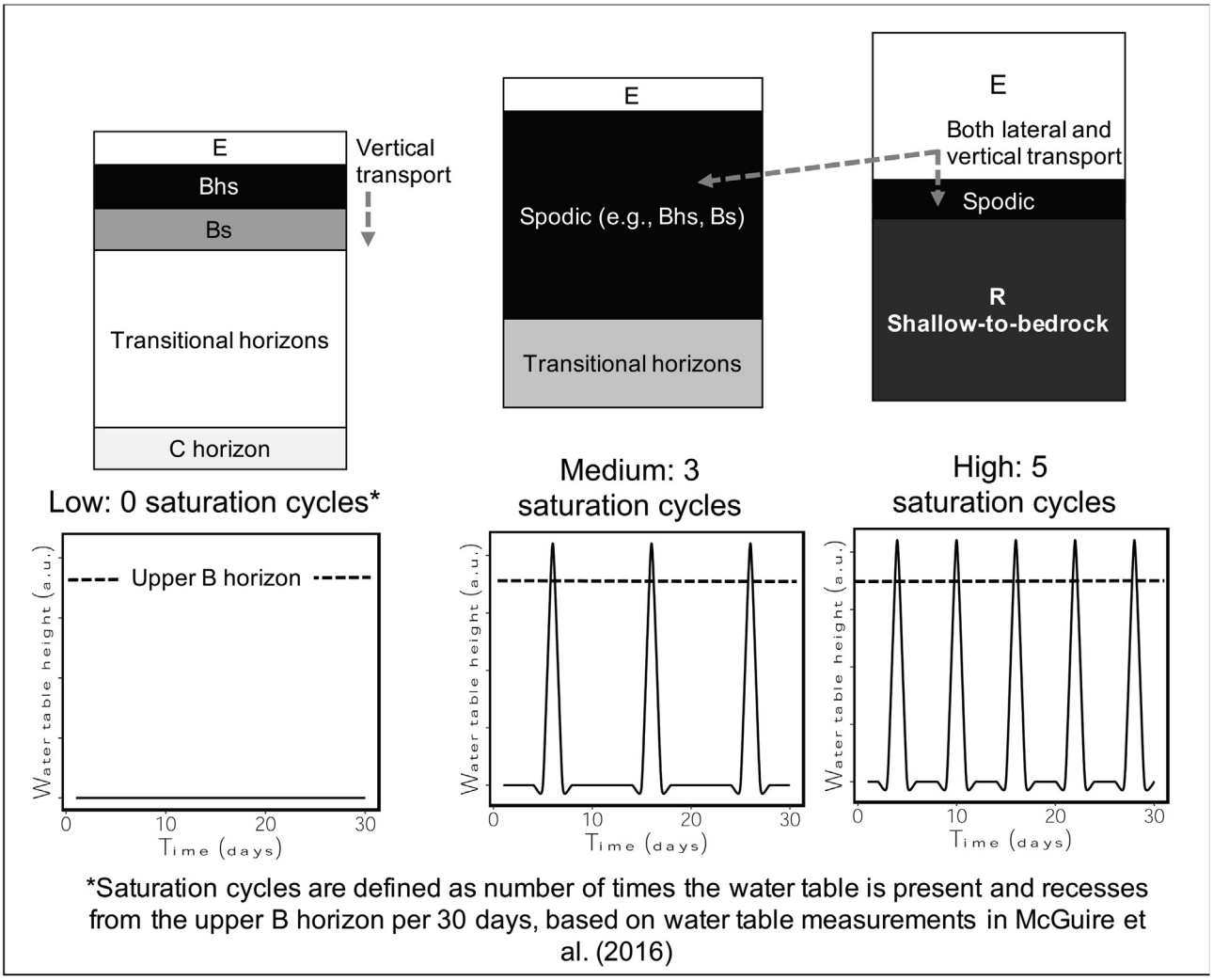


**Fig. 1.** Simplified schematic of variations in mineral soil profile horizons and transport associated with forested Spodosols under variable water table regimes (shown as simplified graphs for illustrative purposes). In this study, categories of saturation cycle frequency (low, medium, and high) were assigned to soil units, previously defined as typical, Bhs, and E podzols, respectively (Bailey et al., 2014; Bourgault et al., 2015, 2017; Gannon et al., 2017). Year-round water table measurements on the same watershed at Hubbard Brook Experimental Forest (Woodstock, New Hampshire) (McGuire et al., 2016) were used to estimate the number of times the water table was present and recessed from the upper B horizon (usually a spodic horizon, e.g. Bhs, Bh, Bs) per 30 days. Eluvial (E horizon) vs. spodic (Bh, Bhs, or Bs) horizon thickness is an example of a distinguishing characteristic between the highest and medium saturation frequency profiles.

indices showed a minor (~35%) increase in coniferous tree basal area with increasing elevation, but white birch (*B. papyrifera*) accounted for the largest proportion of basal area in all sampling locations (Supplementary Table A3). Additionally, the composition of water-extractable organic matter (WEOM) from organic (Oa) horizons was determined to be similar for high and low wet-dry cycling profiles, respectively, using C near-edge X-ray absorption spectroscopy (XANES) (see Supplementary Methods Sections 1.1 and 1.2, Supplementary Fig. A2).

### 2.2. Mineral-organic interaction dynamics

#### 2.2.1. Bulk soil basic soil characterization and metal selective extractions

Bulk soil basic characterization methods (soil pH, total C, and total N) are described in Supplementary Methods 1.3. Total metals were measured using the lithium (Li) meta/tetraborate flux method (Kurtz et al., 2000) (Supplementary Methods 1.3). Acid ammonium oxalate, hydroxylamine-hydrochloride (HCl), and citrate-dithionite extractions were performed in tandem on bulk soils according to standard protocols (Supplementary Methods 1.4). From published extraction efficiencies, we assumed each extractant to target the following pools: (1) hydroxylamine-HCl: organically-complexed, non- and semi-crystalline metals, and minor amounts of crystalline Fe and Al (Ross and Wang, 1993; Shang and Zelazny, 2008); (2) acid ammonium oxalate: pools in (1), and in addition magnetite ($Fe_3O_4$) and minor amounts of trioctahedral Fe and Al (Parfitt and Childs, 1988; Ross and Wang, 1993; Shang and Zelazny, 2008); and (3) citrate-dithionite: pools in (1) and (2), and in addition crystalline metals, but excluding silicate or rock crystalline phases (Parfitt and Childs, 1988; Ross and Wang, 1993).

For a subset of spodic horizons (n = 3 for each saturation frequency) (Supplementary Table A4), a separate hydroxylamine-HCl extraction was completed at a 1:60 w/v soil:extract ratio in order to determine the relative increase in OC, Fe, and Al content of the hydroxylamine extract compared to a water-only extraction (completed at a 1:60 w/v soil:water ratio). We considered the ratio of hydroxylamine-HCl extractable OC to water-extractable organic carbon (WEOC) to correlate to the amount of OC released by dissolution of organically-complexed and semi-crystalline Fe and Al (analogous to methods used in Coward et al., 2017; Heckman et al., 2018). The supernatant OC concentration was measured in solution using a Shimadzu TOC-$V_{CPH/CPN}$ analyzer (combustion method) (Shimadzu Corp, Kyoto, JP). Hydroxylamine-extractable Fe and Al concentrations were

measured in this subset of samples using ICP-atomic emission spectrometry (ICP-AES) (Thermo iCAP 6500 series, ThermoFisher Scientific, Bellafonte, PA) in a 2% nitric acid matrix.

#### 2.2.2. Bulk soil statistical analyses

Differences in spodic horizon total and extractable Fe, Al, and Mn for soils from each saturation frequency category were determined using the non-parametric Kruskal-Wallis test with Dunn test post-hoc comparisons (Bonferroni correction method) in base R (R Core Team, 2017). Additionally, the bulk elemental and extraction data collected for all mineral soil horizons (eluvial, spodic, transitional, and substratum) were used to assess the strongest predictors of total C content across all saturation frequencies. To account for covariation and potential non-linear relationships between soil C and variables, a Random Forest machine learning regression approach was used to compute variable importance rankings using the "caret" and "randomForest" packages in R v. 3.5.3 (Breiman, 2001; Kuhn, 2008; R Core Team, 2017). Further details describing the Random Forest approach are described in Supplementary Methods (Supplementary Methods 1.5).

### 2.3. Probing metal–carbon interactions: Elemental spatial relationships, X-ray absorption and NMR spectroscopy

#### 2.3.1. Elemental spatial relationships

Elemental maps ($^{12}C^{14}N^-$, $^{56}Fe^{16}O^-$, and $^{27}Al^{16}O^-$) of fine-fraction particles for a low and high saturation frequency horizon were collected using nanoscale secondary ion mass spectrometry (NanoSIMS). Imaging was conducted using a Cameca NanoSIMS 50L instrument (Gannevilliers, FR) at the Technical University Munich (Freising, DE). Air-dry soil samples (< 2 mm) were brought to field-moist conditions for a 14-d incubation prior to air-drying for NanoSIMS analysis. Samples were prepared by brief (6-s) low-energy (water bath) sonication of 0.25 g air-dry soil suspended in 10 mL Nanopure® water. After allowing larger particles to settle, a ~100-μL suspension was drop-cast on Si wafers and air-dried. Prior to NanoSIMS imaging, the distribution of particles was characterized and regions of interest (ROI) selected by optical microscopy (Zeiss Axio Imager Z2, Oberkochen, DE) and scanning electron microscopy (JEOL JSM 5900LV, Tokyo, JP), with an ~5 nm-thick gold (Au) sputter coating. For NanoSIMS data collection, a high beam current was applied prior to image collected to remove sputter coating. NanoSIMS ion images (30x30 μm) were collected for $^{12}C^{14}N^-$, $^{27}Al^{16}O^-$ and $^{56}Fe^{16}O^-$ with 1 ms pixel$^{-1}$ dwell time. Images were aligned and summed in the OpenMIMS package (Gormanns et al., 2012) in ImageJ v 2.0.0 (Schneider et al., 2012). For low and high saturation frequency soils, images from multiple regions were analyzed for pixel intensity correlation (n = 5 images for high and n = 4 for low saturation frequency). Pixel intensity correlation between elements (CN-Al, CN-Fe, and Fe-Al) was determined using Spearman rank correlation ($r_s$) in base R (R Core Team, 2017).

#### 2.3.2. Fe K-edge XAS

Changes in bulk Fe speciation across soil saturation frequency were determined for a set of nine spodic and/or transitional (high saturation frequency only) horizons with Fe K-edge X-ray absorption near-edge structure (XANES) and extended X-ray absorption fine structure (EXAFS) (Supplementary Table A4). Fe XAS data were collected at the Cornell High Energy Synchrotron Source (CHESS) F3 hard X-ray beamline (Ithaca, NY) in fluorescence mode, using the energy region of 6912 to 7537 eV to include the pre-edge (−200 to −20 eV), near-edge (−20 to + 12 eV), and post-edge (+12 to + 425 eV) regions relative to the Fe K-edge (7112 eV). The step size was 5 eV for the pre-edge, 1 eV for the near-edge, and 0.05 wavenumber (Å$^{-1}$) for the post-edge, with fixed 1, 2, and 5 s dwell time, respectively. Sample and standard preparation and Fe XANES data collection approaches are described in detail in Inagaki et al. (2020). Briefly, after spectrum normalization and flattening performed using Athena in Demeter v 0.9.25 (Ravel and Newville, 2005), a four Gaussian function model (Inagaki et al., 2020) was used to semi-quantitatively estimate the feature at 7120 eV associated with increasing Fe(II) (1 s–4 s transition) in the first derivative of normalized fluorescence spectrum (Berry et al., 2003). Standards included ferrihydrite (nominally $Fe_2O_3{\cdot}0.5H_2O$), goethite (α-FeO(OH)), nontronite and $Fe^{2+}$-substituted nontronite (Fe-rich smectite), and fayalite ($Fe_2SiO_4$) as mineral standards, and Fe (II) citrate ($C_6H_6FeO_7$), Fe (III) citrate ($C_6H_5FeO_7$), and Fe (III) ethyldiaminetetraacetic acid (EDTA) ($C_{10}H_{12}N_2NaFeO_8$) as Fe-organic complex standards.

Analysis of the Fe XANES first derivative spectra was also conducted with linear combination fitting (LCF) in Athena (Demeter 0.9.25) (Ravel and Newville, 2005; Lengke et al., 2006). A reduced set of standard compounds was selected represent variation in both Fe(II) and Fe-organic bonding: Fe(II) citrate, Fe(III) citrate, ferrihydrite, and $Fe^{2+}$-substituted nontronite. The LCF was performed with component weights constrained to 0–1 and to sum to 1.

To further assess Fe-organic bonding, post-edge EXAFS spectra were K-space transformed for the 3–10 Å$^{-1}$ wavenumber range and plotted as $k^2$-weighted spectra in Athena (Demeter 0.9.25) (Ravel and Newville, 2005). Spectra were qualitatively assessed with emphasis on reduced amplitude at 7.5 Å$^{-1}$ associated with increased Fe-organic bonding in non-crystalline Fe (Chen et al., 2014). Additionally, LCF was applied in Athena for the EXAFS $k^2$-weighted spectra as described for XANES, using goethite, ferrihydrite, and Fe(III) EDTA as crystalline, semi-crystalline, and Fe-organic complex standards, respectively.

#### 2.3.3. Carbon K-edge XANES

The bulk C composition of a subset of the investigated spodic/transitional horizons was determined with C K-edge XANES (Supplementary Table A4). Composition of C in WEOC (Section 2.2.1) and bulk soil with light particulate organic matter (POM) removed was also determined with C K-edge XANES spectroscopy for horizons used for incubation experiments (Section 2.4) (Supplementary Table A4). All C K-edge XANES measurements were conducted at the spherical grating monochromator (SGM) beamline of the Canadian Light Source (Saskatoon, SK), equipped with silicon drift detectors (SDD) for partial fluorescence yield (PFY). The SGM end station was operated under ca.$10^{-6}$ Torr. Further detail on sample preparation and spectral data collection are included in Supplementary Methods Sections 1.2 and 1.6. Damage tests were collected to assess development of spectral artifacts resulting from sample radiation damage (Supplementary Methods 1.7, Supplementary Results and Discussion 2.2).

#### 2.3.4. $^{13}C$ NMR Fe(III) interference experiments

The association between paramagnetic Fe(III) and distinct C forms was probed directly in a subset of bulk soils (Supplementary Table A4) using $^{13}C$ cross-polarization magic angle spinning (CPMAS) nuclear magnetic resonance (NMR) spectroscopy. In brief, this approach estimates the degree of paramagnetic Fe(III) interference on $^{13}C$ NMR signal intensity separately for carboxylic, aromatic, O/N-alkyl, and alkyl C components of the NMR spectrum. In CPMAS NMR, the proton ($^1H$) spin–lattice relaxation time in the rotating frame ($T_{1\rho}H$) is shortened as a result of contact between $^1H$ and paramagnetic centers (Preston et al., 1984); i.e., if Fe(III) interference is present, a negative relationship should exist between $T_{1\rho}H$ and increasing Fe content. The value of $T_{1\rho}H$ was estimated by varying the cross-polarization contact time during $^{13}C$ NMR data acquisition, described in detail in Supplementary Methods 1.8. For these experiments, solid-state CPMAS-$^{13}C$ NMR spectra were collected using a Biospin DSX 200 NMR spectrometer (Bruker, Rheinstetten, Germany) on ball-milled soil samples using a pulse delay of 0.4 s, frequency of 6800 Hz, and accumulation of 100,000 scans. The value of $T_{1\rho}H$ was calculated separately for integrated regions of the NMR spectrum corresponding to carboxylic, aromatic, O/N-alkyl, and alkyl C (Knicker and Lüdemann, 1995) for spodic horizon soil samples (n = 6) across a range of Fe to C ratios. The strength of the relationship between Fe/C and $T_{1\rho}H$ was taken to

indicate the degree of Fe(III) interference, and by extension the degree of medium-range Fe(III)-C interaction for each C functional group (Schöning et al., 2005).

#### 2.3.5. Statistical analyses of spectroscopic results

Differences in Fe K-edge LCF proportions and C K-edge peak height ratios were determined using the non-parametric Kruskal-Wallis rank sum test with post-hoc comparisons with the Dunn test and the Bonferroni correction method in base R (R Core Team, 2017). The effect of the C to Fe ratio on NMR Fe interference was determined using multiple linear regression, with C to Fe ratio and carbon type (alkyl, carboxylic, aromatic, or O/N alkyl) as fixed effects and model F-tests (ANOVA) to determine the significance of model parameters.

### 2.4. Anaerobic-aerobic cycle incubation

For representative soils of high, medium, and low saturation frequency (Supplementary Table A4), macro-POM (defined here as POM > 125 μm able to float in water) was removed prior to incubation by aspiration. Soils suspended in Nanopure® water at a 2:1 water:soil ratio were shaken by hand for 2 min, allowed to settle for < 30 s, and floating material water aspirated. Aspirated solution was returned after sieving to 125 μm and the remaining POM-removed soil was dried at 60 °C.

Water content was determined using a modification of the method described in DeCiucies (2018) modified from Black et al. (1965). Briefly, water content at saturation was determined by saturation of 3–5 g soil overnight in a mesh-lined PVC tube, matching the diameter of the incubation container. After saturation, soil within the PVC tube was allowed to drain freely; after draining of "free" water (1 h), the soil was determined to be at "field capacity" (DeCiucies, 2018).

To drive Fe(III) reduction and determine associated C mobilization and mineralization, a spodic horizon soil from each saturation frequency was incubated for a series of three periods: (1) aerobic only, (2) anaerobic or aerobic, and (3) aerobic only (from here on called "first period, "second period", "third period", respectively). Cumulative carbon dioxide ($CO_2$) for each period was measured using the potassium hydroxide (KOH) trap method (Whitman et al., 2014). A relatively low soil weight (~4 g) was used for incubation to ensure homogenous sample wetting and rapid gas diffusion through the soil sample. Prior to the first incubation period, soils were brought to 50% field capacity and pre-incubated at 30 °C for 2 d in 0.06-L glass vials within 0.4-L glass Mason jars, modified with air-tight septa (n = 4 jars for each soil). At the initiation of each incubation period, 2 mL $CO_2$-free water was added to the jars to maintain a moist environment. For the first period (only aerobic), a KOH trap was added to each jar and the jar was purged for 5 min with $CO_2$-free air (Zero Air Airgas, Inc, Elmira, NY). After this first 5-d period, dissolved $CO_2$ was measured in the KOH trap via changes in electrical conductivity and converted to $CO_2$ absorbed using a standard curve of known volumes of 99.99% $CO_2$ (Airgas, Inc, Elmira, NY) injected via air-tight septa (Whitman et al., 2014; Krounbi et al., 2018). For the second period, anaerobic jars were purged with 99.99% $N_2$ (Airgas, Inc, Elmira, NY) and aerobic jars purged with 100% $CO_2$-free air. After a 7-d anaerobic incubation, cumulative $CO_2$ was determined as above.

After the second period (anaerobic or aerobic control), moist soils (~0.5 g) were sub-sampled in an anaerobic environment ($N_2$ and $H_2$ glove box with < 1 ppm $O_2$), and an extraction with deoxygenated Nanopure® water was performed at a 1:8 w/v soil:water ratio. Extracts were shaken for 2.5 h at medium speed, followed by centrifugation for 30 min at 3000 rpm. The supernatant was decanted and filtered to 0.45 μm (nylon syringe filters, Restek Corporation, Bellafonte, PA) in an anaerobic environment as above. After sub-sampling, jars were capped tightly and stored overnight at 7 °C. After subsampling, all treatments were purged for 10 min with 100% $CO_2$-free air and cumulative $CO_2$ was measured after a third period lasting 5 d under only aerobic conditions.

Water-extractable $Fe^{2+}$, water-extractable OC (WEOC), total Fe, and total Al were quantified in the extracts after the second period as follows. In de-oxygenated water extracts, dissolved $Fe^{2+}$ was determined immediately under anaerobic conditions using the ferrozine colorimetric method (Viollier et al., 2000; Huang and Hall, 2017). Ferrozine reagent (3-(2-pyridyl)-5,6-diphenyl-1,2,4-triazine-*p,p′*-disulfonic acid monosodium salt hydrate) (1 g $L^{-1}$ in 50 mM 2-[4-(2-hydroxyethyl)piperazin-1-yl]ethanesulfonic acid (HEPES) buffer at pH 8) was mixed with supernatant at a 1:10 v/v ratio and absorbance at 562 nm was measured after 60 min incubation. Iron (III) chloride was used as an analytical standard following hydroxylamine-HCl reduction to $Fe^{2+}$. Total dissolved Fe and Al were determined by ICP-AES (Thermo iCAP 6500 series, ThermoFisher Scientific, Bellafonte, PA) in a 2% nitric acid matrix. Water-extractable OC was determined using a Shimadzu TOC-$V_{CPH/CPN}$ analyzer (combustion method) (Shimadzu Corp, Kyoto, JP). All extract measurement values were corrected for soil dry weight and water content after drying the extraction residue (70 °C). For all incubation experiment results, data were tested for normality and $\log_{10}$-transformed to achieve a Shapiro-Wilks test *p*-value > 0.05. Differences in initial aerobic $CO_2$ mineralization (period 1) across saturation frequency were compared by one-way ANOVA. Two-way ANOVA was used to compare WEOC concentration, soluble total Al and Fe, and soluble $Fe^{2+}$ after the second period (anaerobic or aerobic), and cumulative $CO_2$ mineralization normalized to initial WEOC content after the third (aerobic) period. The two-way ANOVA tested the main effects of soil saturation frequency, treatment (anaerobic or aerobic), and their interaction. When main effects with $p < 0.05$ were detected, post-hoc analysis was conducted with Tukey's honest significant difference (HSD) test.

## 3. Results

### 3.1. Mineral-organic interaction dynamics

#### 3.1.1. Basic soil characterization

Overall, soil pH increased in deeper horizons for low and high saturation frequency category soils, but did not change appreciably with depth for medium saturation frequency soils (Supplementary Table A5). For transitional horizons and C horizons, the lack of observations at medium and high saturation frequency precluded comparisons across saturation frequency soils. For eluvial and spodic horizons, pH increased with increasing soil saturation frequency (Supplementary Table A5). Total C and N contents increased in spodic horizons compared to eluvial and transitional/C horizons for low and medium saturation frequency category soils, but did not change appreciably with depth at high saturation frequency (Supplementary Table A5). For eluvial and spodic horizons, C and N content decreased in soils with increasing saturation frequency (Supplementary Table A5).

For spodic horizons, total Fe decreased in high saturation frequency soils (Kruskal-Wallis $p = 0.08$) (Fig. 2). Total Al did not change across soils with varying saturation frequency, resulting in a higher (Kruskal-Wallis $p = 0.08$) ratio of total Al to total Fe in high saturation frequency soils (Fig. 2). For spodic horizons, total Mn did not change across soil saturation frequency categories (Kruskal-Wallis $p = 0.16$, Supplementary Fig. A3, Supplementary Table A5).

#### 3.1.2. Selective extractions

The proportion of total metals extractable by hydroxylamine-HCl (organic complexes and semi-crystalline, excluding magnetite), acid ammonium oxalate (organic complexes and semi-crystalline, including magnetite), and citrate-dithionite (organic complexes, semi-crystalline, and crystalline, excluding aluminosilicates) varied across genetic horizons (Supplementary Table A6). Semi-crystalline mineral contents generally increased in spodic and transitional horizons and decreased in eluvial horizons and substratum (Supplementary Table A6). In spodic

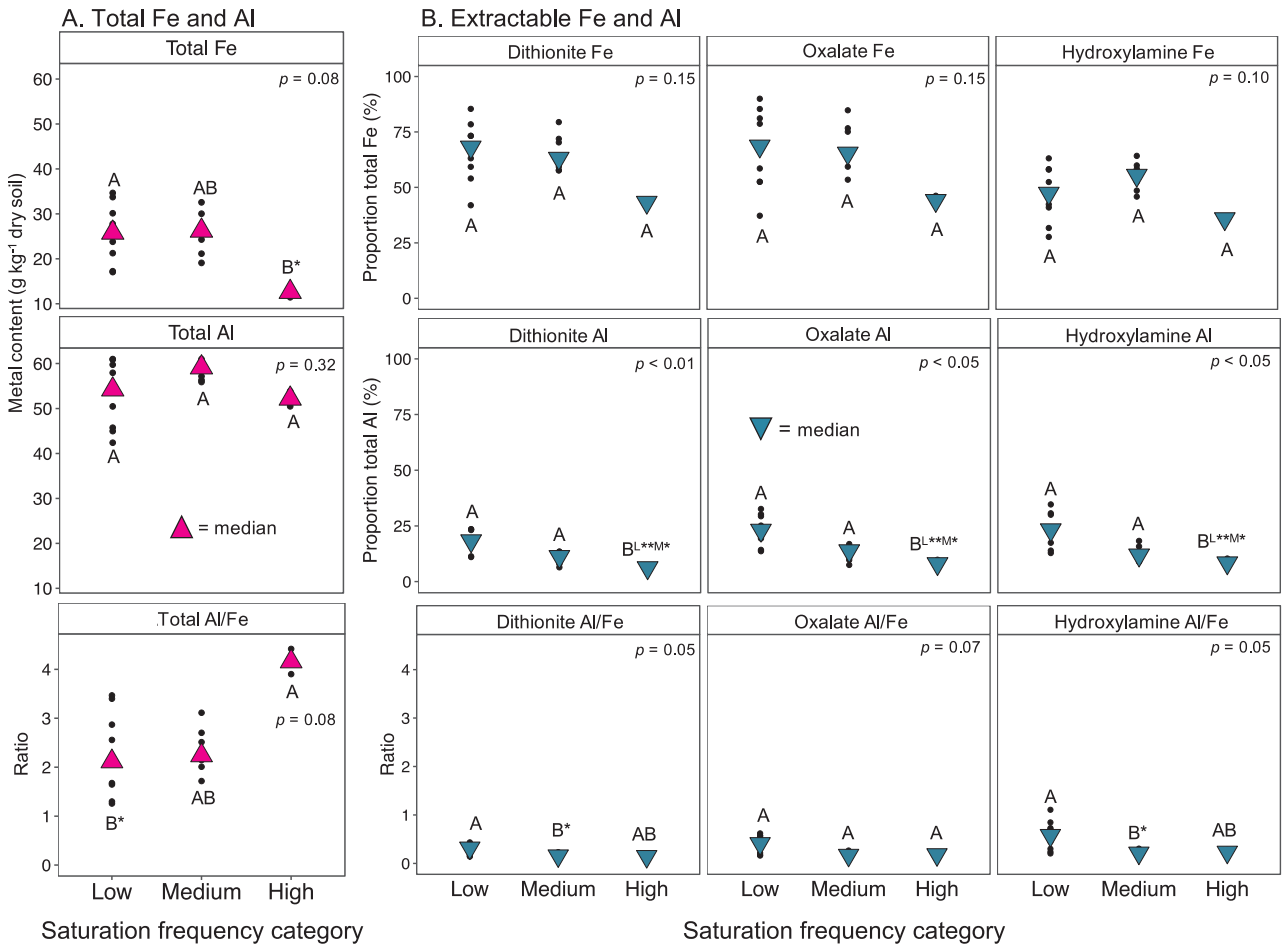


**Fig. 2.** A. Bulk soil total iron (Fe), total aluminum (Al), and Al to Fe ratio for spodic horizon soils from low (n = 8), medium (n = 7), and high (n = 2) saturation frequency categories (defined by the number of saturated–unsaturated cycles in the upper B horizon). B. Bulk soil citrate-dithionite, acid ammonium oxalate, and hydroxylamine-HCl extractable Fe and Al and the ratio of extractable Al/extractable Fe for spodic horizons. For both A and B, points are individual measurements and triangles show the arithmetic median. Within each element and extractant, *p*-values are shown for overall Kruskal-Wallis ANOVA on ranks. Letters show post-hoc multiple comparisons (Dunn Test with Bonferroni correction), with different letters showing significant differences at α = 0.1 (*) and α = 0.05 (**).

horizons, all extractants recovered similar amounts of Fe and Al as a proportion of total Fe and Al (Fig. 2), indicating a minor contribution of magnetite and crystalline phases. The extractable proportion of total Fe was high (up to 60% of total Fe). A weak trend ($p$ = 0.10–0.14) towards lower extractable Fe in high saturation frequency soils was detected (Fig. 2). For hydroxylamine-extractable Fe, a slight increase was observed in medium saturation frequency soils (Fig. 2).

All selective extraction approaches showed a significant decrease in Al in high compared to either low or medium saturation frequency soils (Fig. 2). For all Fe and Al extracts, the ratio of Al to Fe was lower (approximately 1:1 Al/Fe) than for total Al and total Fe (approximately 5:1 Al/Fe). In contrast to total Al/total Fe, the ratio of extractable Al to extractable Fe did not differ between low and high saturation frequency soils for any extract (Fig. 2). However, a decrease in dithionite- and hydroxylamine-extractable Al to Fe ratio was detected for medium saturation frequency soils only (Fig. 2). Extractable Mn (oxalate and hydroxylamine only) was generally low (< 10% of total Mn), but a significant decrease in extractable Mn was detected between soils with low and high saturation frequency (Supplementary Fig. A3).

The amount of OC in hydroxylamine-HCl extracts relative to water extracts (hereafter called "$OC_{HYD}/OC_W$") was of similar magnitude to the ratio of hydroxylamine-extractable to water-extractable Fe ($Fe_{HYD}/Fe_W$) in low saturation frequency soils (Fig. 3). In contrast, the relative magnitude of $OC_{HYD}/OC_W$ was approximately 2.5 times greater than $Fe_{HYD}/Fe_W$ in high saturation frequency soils, but closer in magnitude to $Al_{HYD}/Al_W$ (Fig. 3). For medium saturation frequency soils, the magnitude of $OC_{HYD}/OC_W$ was similar to both $Fe_{HYD}/Fe_W$ and $Al_{HYD}/Al_W$ (Fig. 3).

### 3.1.3. Elemental micro-spatial relationships

Elemental maps derived from NanoSIMS images (Fig. 4) generally showed a high spatial correlation (Spearman Rank correlation coefficient, $r_s$, > 0.5) between Fe-Al, Fe-OM and Al-OM. A tendency towards weaker spatial correlation for Fe-OM and Fe-Al was detected for higher saturation frequency soils, indicating more dispersed elemental distribution (Fig. 4). In contrast, a stronger correlation for Al-OM was detected in higher saturation frequency soils.

### 3.1.4. Mineral soil drivers of total C content

Over 5 independent iterations, the predicted values of the Random Forest regression model were significantly correlated with observed C content (linear regression $R^2 = 0.683, p < 0.005$) (Supplementary Fig. A4). Dithionite/oxalate/hydroxylamine Fe and dithionite/oxalate-extractable Al were consistently (in > 1 model iteration) ranked in the top 5 positions (ranking > ~75) (Table 1). Spodic horizon identity (in contrast to eluvial horizon identity) was also highly ranked. Consistently mid-range (ranking > ~62) variables included pH, volumetric water content, and total Fe. In contrast, extractable and total Mn, low or medium frequency category (in contrast to high saturation frequency), horizon identity other than spodic (in contrast to eluvial horizon identity), total Al, and depth were identified as being of lower (ranking < ~62) importance.

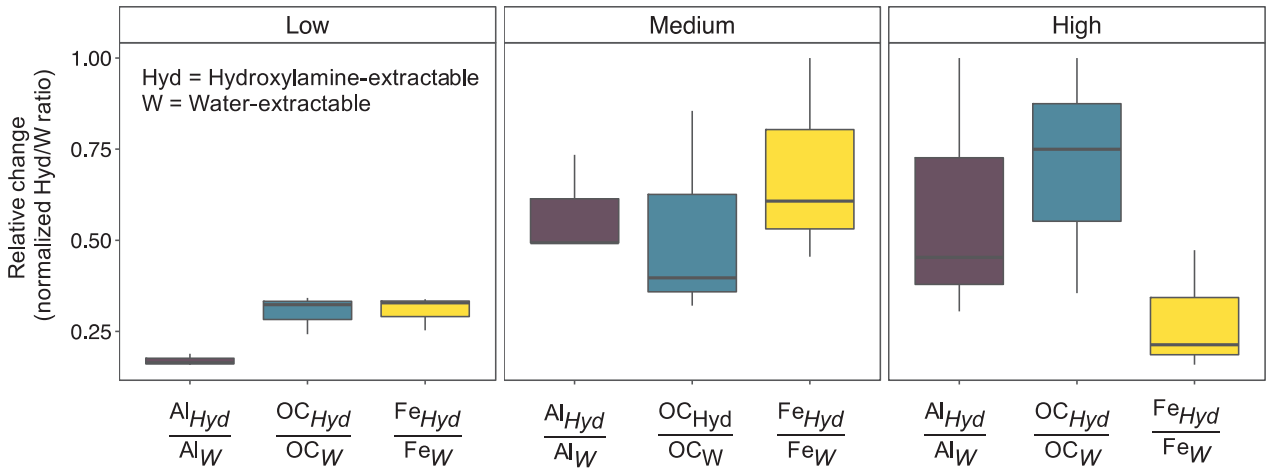


**Fig. 3.** Aluminum (Al), organic carbon (OC), and iron (Fe) released by hydroxylamine extraction ("Hyd") relative to water extraction ("W") for spodic or transitional horizons (n = 3) (listed in Supplementary Table A4) from low, medium, and high saturation frequency category soils (defined by the number of saturated–unsaturated cycles in the upper B horizon). Ratios are normalized (max = 1) within each extracted element (OC, Fe, or Al) to illustrate the relative magnitude of OC co-extracted with hydroxylamine-extractable (i.e., organically complexed and semi-crystalline) Fe or Al. Lower and upper edges of boxes show first and third quartiles (25th and 75th percentiles) and lower and upper whiskers show the smallest and largest value no further than 1.5*interquartile range (IQR) of the box edges.

### *3.2. Probing metal–carbon interactions: X-ray absorption and NMR spectroscopy*

#### *3.2.1. Fe K-edge XAS*

The normalized fluorescence intensity (μE) for Fe standards shifted towards lower energy for the pre-edge centroid, white line, and edge inflection ($E_0$) with increasing reduced Fe and for Fe-organic complexes (Supplementary Table A7). Spodic horizon Fe K-edge spectra did not vary with respect to pre-edge centroid position, but a trend towards lower energy position was detected for the white line position and edge inflection with increasing saturation frequency (~1 eV shift between low and high saturation frequency) (Supplementary Table A7). For the first derivative of normalized μE (dx/dμE), an increase in peak area at 7120.0 eV associated with reduced Fe (1 s–4 s transition) was detected for reduced Fe(II) standards and for soils with increasing saturation frequency (Fig. 5, Supplementary Fig. A5). Soils with high saturation frequency approached the 7120.0 eV peak area of Fe(II)-substituted nontronite (~30% 7120.0 eV area), which contains a mixture of Fe(II) and Fe(III) (Fig. 5).

LCF models for both XANES and EXAFS spectral regions of spodic horizon soils confirmed the increase in reduced Fe components with soils with increasing saturation frequency, and further refine information about Fe composition (Supplementary Fig. A6). Using the XANES LCF model, we detected an increase of Fe(II)-complex and mixed Fe(II)/Fe(III) mineral components in high saturation frequency soils (Supplementary Fig. A6). Semi-crystaline Fe (ferrihydrite) accounted for the highest proportion in the EXAFS LCF model for all saturation frequency soils. We detected a decrease in Fe-organic components and a relative increase in both crystalline and non-crystalline components in higher saturation frequency soils using the EXAFS LCF model, but the differences were not statistically significant ($p \sim 0.4$) (Supplementary Fig. A6). The magnitude of the 7.5 $Å^{-1}$ feature in $k^2$-weighted EXAFS spectra also increased in high saturation frequency soils, an indication of reduced Fe-organic bonding (Chen et al., 2014) (Supplementary Fig. A7). Together, the Fe XANES fine-structure analysis (7120.0 eV peak area) and LCF models indicated a shift in Fe composition from predominantly Fe(III)-organic complexes in low saturation frequency soils towards mixed Fe(II)/Fe(III) mineral phases in higher saturation frequency soils.

#### *3.2.2. Carbon K-edge XANES*

A trend of increasing carboxylic/aromatic C ratio was detected in soils with increasing saturation frequency, with a significantly higher ratio in soils with high vs. low saturation frequency (Kruskal-Wallis $p < 0.05$) (Fig. 6, Supplementary Fig. A8, Supplementary Table A8). The substituted-aromatic/aromatic ratio also increased with saturation frequency. Water-extractable organic matter (WEOM) had a higher carboxylic/aromatic C ratio relative to the bulk soil for low and medium saturation frequency soils, but did not change for high saturation frequency soils (Fig. 6, Supplementary Fig. A8, Supplementary Table A8). Soils with POM removed were also similar in composition to bulk soils, with a slight increase in carboxylic/aromatic C ratio at medium saturation frequency only. Substituted-aromatic/aromatic C ratio was also higher in WEOM and soils with POM removed than in the bulk soil in low and medium saturation frequency soils. In contrast, substituted aromatic/aromatic C was lower in WEOM and POM than the bulk soils in high saturation soils (Fig. 6).

#### *3.2.3. $^{13}C$ NMR estimation of Fe interference*

Medium and short-range OC-Fe(III) interactions can be inferred when proton relaxation time ($T_{1\rho}H$) decreases as a function of increasing Fe content in CPMAS $^{13}C$ NMR (Preston et al., 1984). The effect of Fe/C on relaxation time differed significantly between carbon forms (MLR F-test $p < 0.1$, log-transformed) (Supplementary Fig. A9). The effect size of increasing Fe/C (slope of untransformed $T_{1\rho}H$ vs. Fe/C, given in parentheses) increased in the order alkyl C (−3.7) < O/N alkyl C (−7.3) < aromatic C (−44.4) < carboxylic C (−60.6) (Supplementary Fig. A9). Due to the detection of shorter relaxation times with higher Fe content, aromatic and carboxylic C were inferred to be more strongly affected by Fe(III) interference.

### *3.3. Anaerobic-aerobic cycle incubation*

During the first 5-d aerobic incubation period, $CO_2$ mineralization normalized to total soil C content (from here on called "C mineralizability") increased for soils from low < medium < high saturation frequency categories, in that order (One-way ANOVA $p = 0.09$) (Fig. 7A). During the following 7-d anaerobic incubation period, $CO_2$ mineralization rates only decreased for the low saturation frequency soils, with an approximately 10-fold difference compared to the aerobic

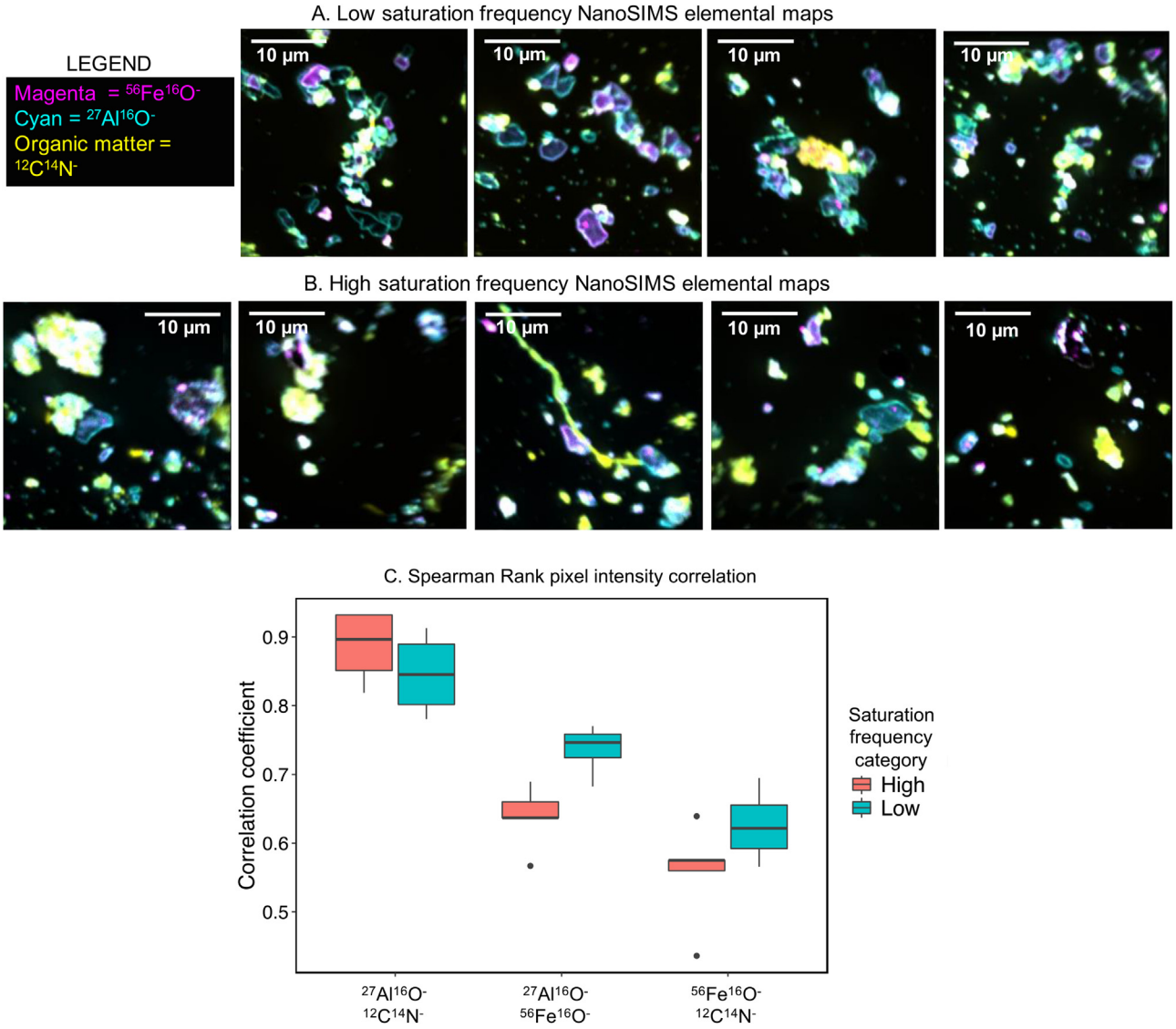


**Fig. 4.** Elemental maps derived from nanoscale secondary ion mass spectrometry (NanoSIMS) imaging showing distribution of iron (as $^{56}Fe^{16}O^-$), aluminum ($^{27}Al^{16}O^-$) and organic matter ($^{12}C^{14}N^-$) for low (A) and high (B) saturation frequency category soils (defined by the number of saturated–unsaturated cycles in the upper B horizon). C. Element spatial correlations (Spearman Rank Correlation) are derived from nanoscale secondary ion mass spectrometry (NanoSIMS) elemental maps. Lower and upper edges of boxes show first and third quartiles (25th and 75th percentiles) and lower and upper whiskers show the smallest and largest value no further than 1.5*interquartile range (IQR) of the box edges. Individual points beyond whiskers are considered outliers.

treatment; however, two-way ANOVA main effects were not significant (Table 2). After the second period, WEOC (as a proportion of total C) and Al did not change under anaerobic incubation compared to the aerobic incubation for soils from all saturation frequencies (Table 2). In contrast, both water-extractable total Fe and $Fe^{2+}$ as a proportion of total soluble Fe increased after the anaerobic incubation period (ANOVA main effect $p = 0.08$ and $p = 0.07$) for all saturation frequency soils (Table 2). While the WEOC amount did not increase after the anaerobic period, cumulative $CO_2$ mineralized in the third aerobic period divided by the initial WEOC amount (hereafter termed "WEOC mineralizability") increased significantly after an anaerobic incubation period for the high saturation frequency soil only (Tukey HSD $p < 0.005$ for comparison to aerobic control) (Fig. 7B). Differences in WEOC mineralizability and soluble $Fe^{2+}$ after anaerobic incubations relative to aerobic controls increased in magnitude with increasing saturation frequency (Fig. 7C).

## 4. Discussion

### 4.1. Contrasting mineral-organic interactions across variable saturation frequency soils

In this study, increases in the ratio of bulk soil Al to Fe (Fig. 2), OC release of similar magnitude to Al with selective dissolution (Fig. 3), and Al-SOM spatial associations in the fine fraction (Fig. 4) point towards a shift from Fe- to Al-dominated mineral-SOC interactions in higher saturation frequency soils. In the same study system, increasing Al to Fe ratios in higher saturation frequency soils have been identified in other areas of the watershed (e.g., in Bhs podzol spodic horizons) (Bourgault et al., 2015). In other Fe and Al-dominated systems (Andisols), a shift towards Al-mediated SOC stabilization in wetter soil profiles has been attributed to long-term Fe depletion (Inagaki et al., 2020). At the continental US scale, a stronger correlation between OC content and oxalate-extractable Al than between OC and Fe was identified in very humid systems (Rasmussen et al., 2018), possibly due to long-term Fe loss. Collectively, the relative importance of Al-SOC

**Table 1**
Variable importance rankings (100 = highest rank) for 5 independent Random Forest regression models testing predictor variables of total carbon content. Abbreviations: H = hydroxylamine-hydrochloric acid (HCl)-extractable metal (% total), O = acid ammonium oxalate-extractable metal (% total), D = citrate-dithionite extractable metal (% total), Vol. water = volumetric water content ($m^3$ water $m^{-3}$ soil) at time of sampling, Spodic/Transitional = horizon type, and Low SF = low saturation frequency identity. E horizon and high saturation frequency are categorical variable reference levels.

| Iteration 1 | Rank | Iteration 2 | Rank | Iteration 3 | Rank | Iteration 4 | Rank | Iteration 5 | Rank |
|---|---|---|---|---|---|---|---|---|---|
| Fe-D | 100 | Fe-O | 100 | Fe-D | 100 | Fe-D | 100 | Fe-H | 100 |
| Al-O | 94.3 | Fe-D | 96.0 | Al-D | 98.0 | Fe-O | 894 | Al-D | 97.8 |
| Fe-H | 90.9 | Fe-H | 90.6 | Al-O | 87.8 | Al-D | 87.2 | Fe-D | 97.8 |
| Al-D | 90.4 | Al-D | 84.3 | Fe-H | 87.5 | Spodic | 84.2 | Fe-O | 964 |
| Total Fe | 89.9 | Al-O | 76.9 | Spodic | 86.9 | Fe-H | 83.1 | Al-O | 78.1 |
| Fe-O | 89.8 | Al-H | 71.8 | Fe-O | 84.0 | Total Fe | 71.1 | pH | 74.7 |
| Spodic | 89.3 | Total Fe | 71.1 | Al-H | 78.1 | Al-O | 70.6 | Vol. water | 74.2 |
| Mn-O | 79.4 | pH | 66.4 | Total Fe | 75.6 | Vol. water | 63.1 | TotalFe | 71.2 |
| Al-H | 76.3 | Vol. water | 64.1 | pH | 72.2 | Al-H | 62.2 | Spodic | 66.6 |
| pH | 66.9 | Spodic | 61.6 | Mn-O | 69.5 | Transitional | 61.6 | Low SF | 52.4 |
| Vol. water | 57.5 | Depth | 61.4 | Transitional | 58.9 | pH | 60.5 | Transitional | 52.0 |
| Depth | 52.9 | Total Mn | 48.0 | Total Mn | 58.6 | Low SF | 48.6 | Mn-O | 50.5 |
| Transitional | 41.7 | Mn-H | 47.8 | Vol. water | 56.5 | Depth | 48.0 | Mn-H | 43.8 |
| Substratum | 41.0 | Transitional | 44.4 | Depth | 46.7 | Total Mn | 47.0 | Al-H | 36.2 |
| Total Mn | 32.1 | Total Al | 43.4 | Low SF | 45.6 | Substratum | 44.4 | Depth | 23.6 |
| Mn-H | 23.9 | Substratum | 33.7 | Substratum | 37.2 | Mn-O | 41.7 | Substratum | 18.1 |
| Low SF | 17.6 | Mn-O | 30.3 | Total Al | 37.2 | Mn-H | 13.8 | Med SF | 15.4 |
| Total Al | 8.6 | Med SF | 21.2 | Mn-H | 33.6 | Total Al | 7.7 | Total Mn | 6.9 |
| Med SF | 0 | Low SF | 0 | Med SF | 0 | Med SF | 0 | Total Al | 0 |

interactions with increased saturation and long-term Fe depletion is an emergent consideration for predicting SOC stabilization.

In the absence of ecosystem-scale variability in climate, pH, and parent materials, the shift towards Al-associated organic matter observed in this study is likely driven by direct and indirect effects of Fe reduction on localized soil solution chemistry. For instance, higher pH (~0.5 pH units) observed in high saturation frequency soils (Supplementary Table A5) may be a result of long-term $H^+$ consumption by Fe reduction reactions (Thompson et al., 2006a). Additionally, reduction of Fe(III)-organic complexes may result in increased solubility of organic complexing compounds that are available for reaction with Al and subsequent precipitation. In addition to surface adsorption and complex formation, the co-precipitation of Al with OM is also a likely pathway of organo-Al stabilization (Scheel et al., 2007). With the majority of organo-mineral co-precipitation studies focused on Fe (e.g., Chen et al. 2014, Chen et al. 2016), the critical role of Al observed here in high saturation frequency soils points to the need for further focus on drivers of Al solubility and reactivity.

In addition to Fe and Al, redox transformations of Mn may influence SOC mobilization (Jones et al., 2018). While reactive Mn decreased with increasing saturation frequency, the explanatory power of all Mn variables (total and extractable) for prediction of total C was low (Table 1), suggesting that Mn did not influence C accumulation to the same extent as Fe and Al. Bourgault et al. (2015) identified differences in Mn composition for similar podzol soil units of varying saturation frequency in the Hubbard Brook Experimental Forest, but high spatial variation in Mn content was also identified on the watershed scale. Our observations suggest that the importance of Mn-mediated SOC

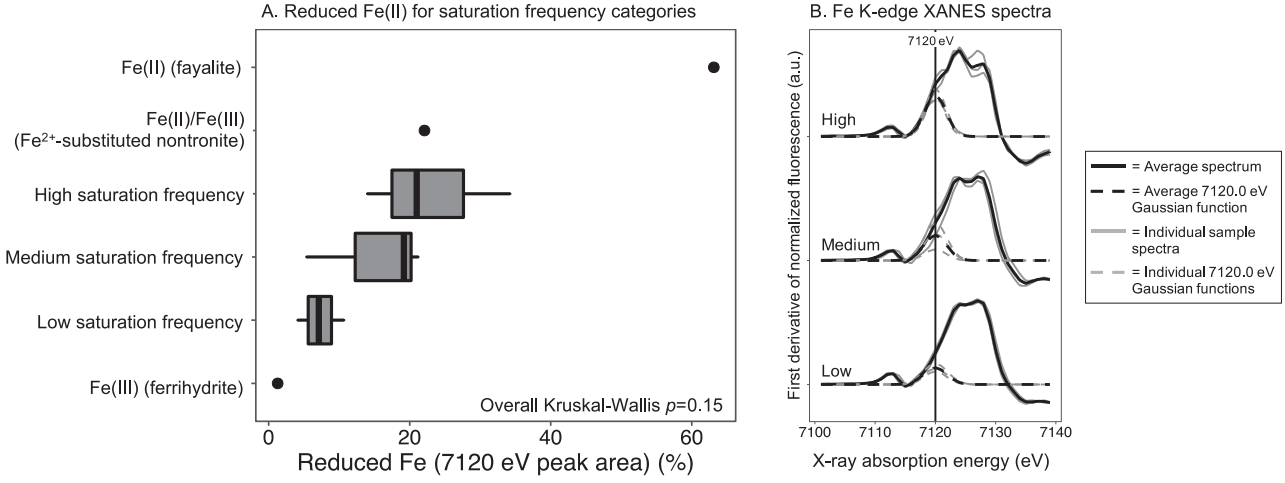


**Fig. 5.** Iron K-edge X-ray absorption near-edge structure (XANES) oxidation state determination for soils across saturation frequency categories (low, medium, and high) (defined by the number of saturated–unsaturated cycles in the upper B horizon). Reduced Fe(II) is shown by proxy as the area of the 7120.0 eV Gaussian function (A) in the XANES first derivative spectrum (B) associated with the 1 s-4 s transition (Berry et al., 2003). In A, boxplots show the distribution of the peak area at 7120.0 eV for spodic or transitional horizons (n = 3) (listed in Supplementary Table A4), with a weak trend towards higher peak area in high saturation frequency soils (Kruskall-Wallis $p$ = 0.15). For reference, the area at 7120.0 eV of standard compounds is included to represent a range of Fe oxidation states, from mostly Fe (III) in ferrihydrite to mostly Fe(II) in fayalite, with Fe(II)-substituted nontronite a mixture of Fe(III) and Fe(II) (data from Inagaki et al., 2020, Appendix A). Lower and upper edges of boxes show first and third quartiles (25th and 75th percentiles) and lower and upper whiskers show the smallest and largest value no further than 1.5*interquartile range (IQR) of the box edges. In B, the solid lines show the average (black) and replicate soil sample (grey) first derivative of normalized fluorescence for each saturation frequency category, and the dotted lines show the average (black) and replicate (grey) Gaussian functions at 7120.0 eV.

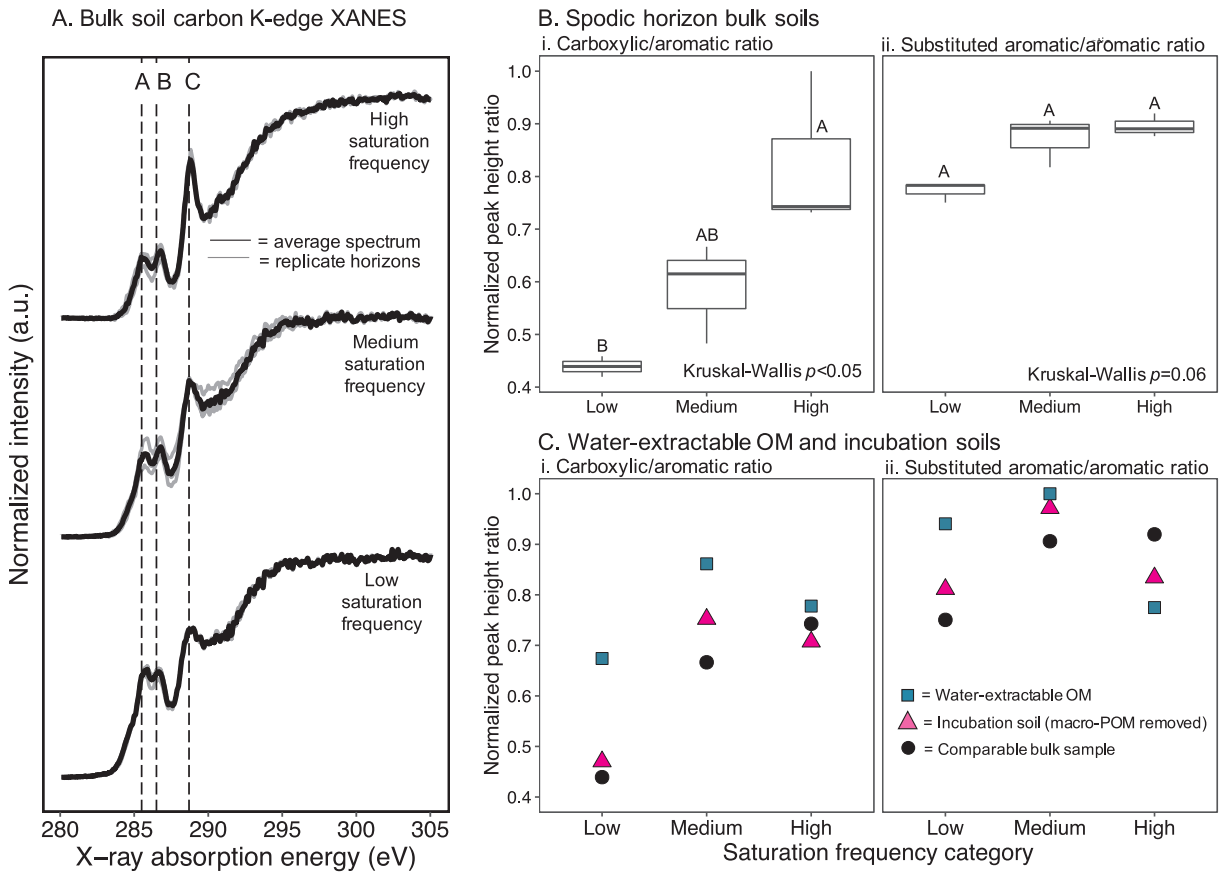


**Fig. 6.** A. Carbon (C) K-edge X-ray absorption near-edge structure (XANES) spectra for bulk soils with varying saturation frequency categories (defined by the number of saturated–unsaturated cycles in the upper B horizon), normalized to edge step = 1 and unsmoothed. Vertical lines A, B, and C indicate aromatic (285.5 eV), substituted aromatic (286.5 eV), and carboxylic (288.7 eV) C features, respectively. B. Normalized (max = 1) peak height ratios of carbon (C) K-edge XANES spectra. For B, boxplots represent the distribution of measurements from spodic or transitional horizons (n = 3 for each saturation frequency, Supplementary Table A4). Lower and upper edges of boxes show first and third quartiles (25th and 75th percentiles) and lower and upper whiskers show the smallest and largest value no further than 1.5*interquartile range (IQR) of the box edges. For C, points show individual measurements comparing bulk soils with water-extractable organic matter (WEOM) extracted from the same soil, and the soil with macro-particulate organic matter (POM) removed by water flotation. Spectra for WEOM and POM-removed soil shown in Supplementary Fig. A9.

stabilization may be localized to areas with Mn enrichment. Additionally, the near order of magnitude difference in Mn content compared to Fe and Al may preclude identification of Mn-SOC interactions occurring on the micron-resolution scale (Jones et al., 2018).

### 4.2. Mechanisms of organo-mineral interactions

#### 4.2.1. Iron mineral composition changes induced by higher saturation cycle frequency

The observed shift towards higher Fe(II) in higher saturation frequency soils suggests that the legacy saturation frequency in this system was sufficient to induce reducing conditions, which resulted in not only mobilization and Fe depletion, but also increased Fe(II) in residual mineral phases (Fig. 5, Supplementary Fig. A6). These shifts were reflected in increasing Fe(II)-organic complex, decreasing Fe(III)-organic complex, and increasing Fe(II)/Fe(III) mineral content in higher saturation frequency soils (Supplementary Fig. A6). The absence of fully reduced Fe(II) phases that form under long-term saturation (e.g., Fe(II) silicates or sulfides) (Prietzel et al., 2007) highlights the distinction between Fe transformations under persistent vs. flashy saturation events.

In this study, an overall shift towards lower Fe-organic complex content in higher saturation frequency soils provides evidence for effects of rapid saturation fluctuations on Fe mineral crystallinity in addition to redox state. This shift is supported by a weak ($p$ = 0.10–0.14) trend towards lower extractable Fe as a proportion of total Fe (Fig. 2), an approximately 50% decrease in Fe-organic and 25% increase in crystalline Fe relative to low saturation frequency soils (Supplementary Fig. A6), and qualitative changes in EXAFS features related to reduced Fe-organic bonding (Supplementary Fig. A7). The proportion of semi-crystalline Fe also increased at high saturation frequency, suggesting that the relative increase in overall crystallinity is due to loss of amorphous Fe-organic phases (Supplementary Fig. A6). Increasing Fe crystallinity with redox fluctuations was identified by Thompson et al. (2006b, 2011) with laboratory wet-dry cycles and in the field across a rainfall gradient in basaltic soils. Using aerobic-anaerobic incubation experiments, Ginn et al. (2017) and Barcellos et al. (2018) showed increased Fe reduction rates with rapid redox fluctuations, and proposed that recently-precipitated Fe(III) is more susceptible to subsequent reduction. This conclusion is supported by increased Fe reduction rates of Fe(III) recently co-precipitated with C in model systems (Chen and Thompson, 2018) and lower-crystallinity Fe (III) in soils (Chen et al., 2018; Vermeire et al., 2019). Consequently, increased reducibility of recently-precipitated Fe(III)-organic complexes and subsequent Fe(II) mobilization provides a possible mechanism for the observed shift towards lower organically-complexed Fe in high saturation frequency soils in this study. A trend towards increased semi-crystalline and/or organically complexed Fe

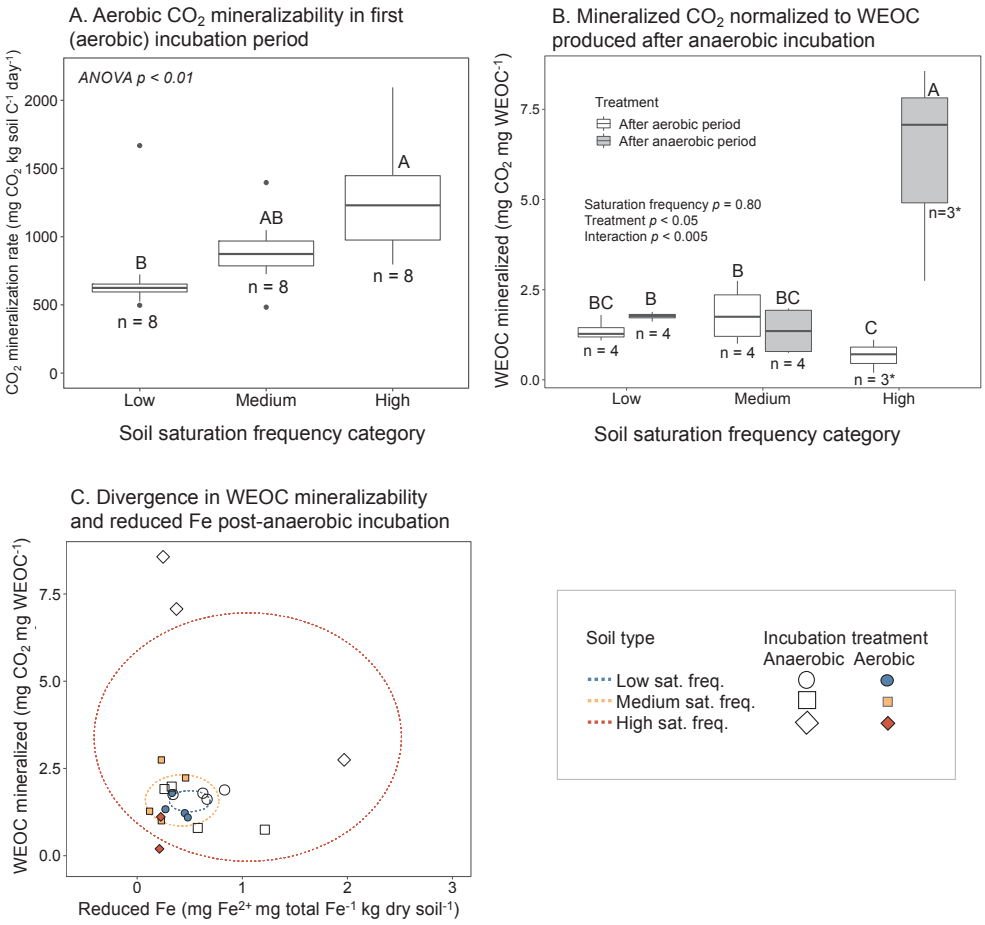


**Fig. 7.** Carbon and water-extractable organic carbon (WEOC) mineralizability as affected by anaerobic incubation for representative soils from high, medium, and low saturation frequency categories (defined by the number of saturated–unsaturated cycles in the upper B horizon). A. Initial carbon dioxide ($CO_2$) mineralizability during the initial 5-d aerobic incubation period (normalized to total soil carbon content). B. Cumulative $CO_2$ mineralized during a final 6-d aerobic incubation, normalized to the WEOC amount extracted after either a previous 7-d anaerobic or aerobic (control) incubation period (i.e., "WEOC mineralizability"). For both A and B, boxplots show the distribution of replicate experimental units. Lower and upper edges of boxes show first and third quartiles (25th and 75th percentiles) and lower and upper whiskers show the smallest and largest value no further than 1.5*interquartile range (IQR) of the box edges. Significant differences (two-way ANOVA) from the highest value at $\alpha = 0.10$ are indicated by different letters. * = one replicate excluded due to WEOC below detection. C. Divergence in WEOC mineralizability and soluble reduced iron (Fe) between anaerobic or aerobic (control) incubations. Circles are centered at the mean of each saturation frequency soil, with radius equal to standard deviation in both X and Y. Increasing circle size illustrates the increasing difference in water extract composition between anaerobic and aerobic treatments with increasing saturation frequency.

**Table 2**
Average carbon dioxide ($CO_2$) mineralization rate change, soluble iron (Fe), soluble aluminum (Al), soluble $Fe^{2+}$, and water-extractable organic carbon (WEOC) following incubation with either anaerobic (anaer.) or aerobic (aer.) conditions. Mineralization rate change was calculated relative to initial respiration rates (Fig. 7). Tukey HSD multiple comparisons are shown when ANOVA main effects have $p < 0.05$. Different letters indicate significant differences at $p < 0.1$ unless otherwise noted.

| | | $CO_2$ mineralization rate change (%) | | Soluble Fe (% total Fe) | | Soluble Al (% total Al)* | | Reduced Fe (% soluble Fe)* | | WEOC (g WEOC kg SOC$^{-1}$)* | |
|---|---|---|---|---|---|---|---|---|---|---|---|
| Saturation Freq. | | Anaer. | Aer. | Anaer. | Aer. | Anaer. | Aer. | Anaer. | Aer. | Anaer. | Aer. |
| Low | Avg | 5.9 | 98.3 | $0.11^{A}$ | $0.06^{A**}$ | $0.09^{A}$ | $0.10^{A}$ | 0.6 | 0.4 | 5.96 | 7.07 |
| | SD | 24.1 | 43.8 | 0.06 | 0.02 | 0.03 | 0.03 | 0.2 | 0.1 | 1.22 | 1.42 |
| | n | 4 | 4 | 4 | 4 | 4 | 4 | 4 | 4 | 4 | 4 |
| Medium | Avg | 49.0 | 89.7 | $0.02^{B}$ | $0.01^{B}$ | $0.02^{B}$ | $0.02^{B}$ | 0.6 | 0.3 | 6.30 | 6.89 |
| | SD | 49.8 | 99.8 | 0.002 | 0.005 | 0.001 | 0.003 | 0.4 | 0.1 | 1.05 | 2.29 |
| | n | 4 | 4 | 4 | 4 | 4 | 4 | 4 | 4 | 4 | 4 |
| High | Avg | 77.5 | 45.1 | $0.01^{B}$ | $0.008^{B}$ | $0.002^{B}$ | $0.002^{B}$ | 1.7 | 0.3 | 1.75 | 14.42 |
| | SD | 128.9 | 111.7 | 0.003 | 0.003 | 0.001 | 0.001 | 1.8 | 0.05 | 0.95 | 18.02 |
| | n | 4 | 4 | 4 | 4 | 4 | 4 | 4 | 3 | 3 | 3 |
| Main effects | DF | F stat | *p*-value | F stat | *p*-value | F stat | *p*-value | F stat | *p*-value | F stat | *p*-value |
| Treatment (anaerobic vs. aerobic) | 1 | 0.92 | 0.35 | 3.48 | 0.08 | 4.8E-05 | 0.15 | 3.69 | 0.07 | 2.14 | 0.16 |
| Saturation frequency | 2 | 0.08 | 0.92 | 25.33 | 5.9E-06 | 67.2 | 4.49E-09 | 1.43 | 0.27 | 0.12 | 0.89 |
| Interaction effect | 2 | 1.07 | 0.36 | 2.15 | 0.15 | 0.09 | 0.92 | 1.28 | 0.30 | 1.80 | 0.20 |

*When log transformation resulted in Shapiro-Wilks $p < 0.05$, the p-value was used as the conservative level of significance. Soluble Al $\alpha = 0.03$, reduced Fe $\alpha = 0.03$, DOC $\alpha = 0.006$. **p = 0.1.

(hydroxylamine-extractable) at medium saturation frequency (Figs. 2 and 3) may also be attributed to lateral transport of mobile Fe(II) from high saturation frequency soils and subsequent re-precipitation.

#### 4.2.2. Iron-carbon and aluminum-carbon interactions

By pairing imaging and bulk extraction approaches with analysis of organo-mineral bonding (e.g., Fe K-edge XAS and $^{13}C$ NMR Fe interference experiments), the presented dataset can be used to infer mechanisms of metal-C interaction. High contents of carboxylic acid and

oxidized aromatic functional groups (e.g., oxidized aromatic/aromatic ratio > 0.7) (Fig. 6) and interactions between Fe(III) and carboxylic acids (Supplementary Fig. A9) point towards the role of oxidized SOC in organo-mineral associations. Preferential interaction of carboxylic and/or aromatic acid functional groups with reactive Fe and Al phases has been demonstrated across a wide range of soil types, including semi-crystalline mineral-dominated soils (e.g., Andisols) (Kramer et al., 2012), forest soils of varied soil orders (Zhao et al., 2016), and specifically for Northeast spodic horizons (Ussiri and Johnson, 2004).

While our NMR measurements did not probe Al interactions with SOC directly, similar complexation and surface adsorption reactions with carboxylic and aromatic acids are expected for reactive Fe and Al minerals (e.g., inner-sphere substitution reactions) (Kleber et al., 2015). The particularly high carboxylic C content observed in high saturation frequency soils (carboxylic/aromatic ratio > 0.7) suggests carboxylic acid interactions also contribute to overall Al-C interactions. In addition to the legacy of saturation frequency, differences in SOC composition at the sampling site could theoretically also be a function of secondary influences on soil formation, including differences in organic input composition. However, water extracts from Oa horizons from high and low saturation frequency soils were similar in composition, with a slight enrichment (18%) in carboxylic acid C at the high saturation frequency site (Supplementary Fig. A2), compared to an 89% increase in the bulk soil (Fig. 6). Further, the difference in carboxylic/aromatic C ratio between soils with or without removal of macro (> 125 μm) particulate organic matter (POM) was relatively small irrespective of saturation frequency (Fig. 6). This suggests that the enrichment of oxidized C in high saturation frequency soils was likely due to carboxylic C accumulation via stabilizing interactions (e.g., Al-organic interactions) rather than differences in composition of the C input. However, due to the potential role of heavier, smaller POM (i.e., POM that was not accounted for in C XANES measurements), further isolation of Al-associated C phases and analyses analogous to NMR Fe interference experiments are needed to directly probe Al-C interactions. While the frequency of water table fluctuations is considered the primary driver of soil pedogenesis in this system (Bailey et al., 2014), exploring additional ecosystem variables in future studies will also refine understanding of SOC compositional changes and especially Al-SOC interactions as a function of saturation frequency.

### 4.3. Implications for SOC mineralizability

Changes in Fe redox state (Fig. 5), Fe vs. Al-organic spatial associations (Fig. 4), and bulk OC composition (Fig. 6) in higher saturation frequency soils provides support for redox-driven changes to organo-mineral associations with potential impact on OC mineralization. The shifts in Fe, Al, and C composition detected here suggest that OC stabilization is occurring via different mechanisms that may respond differently to fluctuating saturation and resulting redox conditions. While translating results from laboratory incubations to field settings is challenging (Torn et al., 2009), the controlled incubation conditions employed here may allow for comparison of potential $CO_2$ mineralization across soils with natural variation in saturation frequency. In contrast to previous studies that found no increased $CO_2$ mineralization after repeated wet-dry cycling (Degens and Sparling, 1995), we identified an increase of total C mineralizability (ANOVA $p = 0.09$) in soils with a legacy of high saturation frequency after 5-day aerobic incubation. With Fe and Al shown to be important drivers of SOC accumulation via mechanisms described above, the detected increase in total C mineralizability (Fig. 7, Table 2) may be associated with the shift from Fe(III) to Al-dominated organo-mineral interactions.

The nature and stability of SOC-metal interactions are not expected to be categorically different between Al and Fe, as such, due to the potential for stabilizing interactions with both elements via complex formation and co-precipitation (Basile-Doelsch et al., 2007; Kalbitz and Kaiser, 2008). However, the potential for SOC-Al interactions resulting in decreased SOC mineralizability may be more pronounced for higher solubility Al phases compared to crystalline Al (Kalbitz and Kaiser, 2008). Here, non-crystalline Al as a proportion of total Al was lower (< 25%) than non-crystalline Fe as a proportion of total Fe at all sites (> 25%), and especially in high saturation frequency soils (Fig. 2). While the reactive Al present may account for a large proportion of organo-mineral associations and confer SOC stabilization, SOC may be in excess of reactive Al surface area in high saturation frequency soils. Consequently, soils that developed at high saturation frequency may be closer to SOC saturation (as described by Six et al., 2002) than those developed under lower saturation frequencies. However, this concept does not account for interactions that are not limited by surface area (e.g., co-precipitation and additive accumulation of SOC) (Vogel et al., 2014).

In high saturation frequency soils, the significant increase in $CO_2$ evolution (normalized to the amount of WEOC) after anaerobic incubation indicates that redox processes remain an influence on SOC cycling, despite the observed shift towards Al-dominated interactions. With anaerobic incubation, the overall increase in both soluble total Fe and $Fe^{2+}$ demonstrated the induction of reducing conditions. Since we did not analyze the adsorbed (e.g., dilute HCl-extractable) pool of $Fe^{2+}$, these changes may be underestimated. In incubated high saturation frequency soils, the increase in $Fe^{2+}$ with anaerobic conditions was higher (5-fold) than that for low saturation frequency soils (1-fold). This observation suggests that despite a shift towards Al-dominated organo-mineral interactions and already increased Fe(II) as a proportion of total Fe, Fe redox dynamics remain relevant and a potential influence on WEOC availability.

The potential for SOC mobilization due to the reduction of Fe-associated SOC has been previously observed in soil types with a similarly high abundance of semi-crystalline Fe phases (e.g., Andisols) (Buettner et al., 2014). Hall et al. (2018) also provided evidence for more rapid cycling of C associated with more easily reduced, non-crystalline Fe phases. However, we did not detect an increase in WEOC for any saturation frequency, possibly due to rapid C assimilation by anaerobic microorganisms, precipitation with soluble $Fe^{2+}$, or rapid adsorption to remaining solid Fe and Al phases. While increased soluble OC under wet-dry cycling or flooding has been identified in both organic and mineral soils (Lundquist et al., 1999; Chow et al., 2006), the increase in OC was not necessarily linked with increased microbial respiration and microbial biomass (Lundquist et al., 1999). This contrast highlights the distinction between increased soluble OC amount and OC mineralizability. Soluble OC mineralizability may be influenced by the factors such as composition of original SOC and availability of other limiting nutrients (Kalbitz et al., 2003; Wieder et al., 2008; Petrone et al., 2009). In this study, the observation of lower WEOC amounts with higher mineralizability (i.e., high $CO_2$ mineralized normalized to WEOC) provides an incentive for further studies focused on composition and fate of OC released from mineral associations, particularly with respect to the stabilizing elements (Fe vs. Al) and interaction mechanisms.

## 5. Conclusions

The extent of saturation frequency and hydrology-driven pedogenic processes in this system resulted in notable shifts in Fe redox state and in the composition of Fe phases, underscoring the influence of redox fluctuations even in short-duration, flashy saturation events. The observed transition from Fe(III)-organic interactions in lower saturation frequency soils towards Al-dominated interactions in higher saturation frequency soils indicates relevant changes in potential SOC stabilization mechanisms between nearby locations. This will likely also apply to different locations within the same soil profile, such as between depths or between pores and interiors of aggregates. The higher WEOC mineralizability in response to short-term changes in redox conditions over several days suggests that this shift is relevant for SOC accumulation and stabilization processes. This should be accounted for in

modeling SOC stabilization potential in systems with frequent redox fluctuations. Future research should extend investigations to fine-scale spatial analyses that may capture elemental associations that vary on the fine scale (e.g., Mn-organic associations) and to in-field observations of real-time fluctuations of OC mobilization, composition, and metal solubility at high temporal resolution.

## 6. Data availability

Data associated with this manuscript are published in a Cornell University Ecommons repository entitled: "Carbon and metal characterization and incubation studies conducted on soil samples collected in June 2016 from Hubbard Brook Experimental Forest", available at: https://doi.org/10.7298/412j-t911

## Declaration of Competing Interest

The authors declare that they have no known competing financial interests or personal relationships that could have appeared to influence the work reported in this paper.

## Acknowledgements

Funding for this study was provided by the NSF IGERT in Cross-Scale Biogeochemistry and Climate at Cornell University (NSF Award #1069193) and the Institute for Advanced Study (IAS) from the Technical University of Munich (TUM) through the Hans-Fisher Senior Fellowship. Additional research funds were provided by the Andrew W. Mellon Foundation and the Cornell College of Agriculture and Life Sciences Alumni Foundation, USA. Hubbard Brook Experimental Forest is operated and maintained by the US Forest Service, Northern Research Station, Newtown Square, PA, USA. This work uses research conducted at the Cornell High Energy Synchrotron Source (CHESS) which is supported by the National Science Foundation under award DMR-1332208. Research was performed at the Canadian Light Source (CLS), which is supported by the Canada Foundation for Innovation, Natural Sciences and Engineering Research Council of Canada, the University of Saskatchewan, the Government of Saskatchewan, Western Economic Diversification Canada, the National Research Council Canada, and the Canadian Institutes of Health Research, Canada. The authors thank Dr. Rong Huang of CHESS, Dr. Tom Regier of CLS, Kelly Hanley and Akio Enders of Cornell University for technical assistance; Dr. Carmen Höschen, Johann Lugmeier and Dr. Carsten Mueller of the Technical University of Munich for their support with the NanoSIMS measurements; Dr. Carmen Enid Martinez' research group for providing iron XAS standard materials; Dr. Linda Pardo, Stephanie Duston, Brittany LeBeau, and Johali Sotelo for soil sample collection and field characterization; and the referees for their invaluable insights.

## Appendix A. Supplementary data

Supplementary data to this article can be found online at https://doi.org/10.1016/j.geoderma.2020.114483.

## References

Bailey, S.W., Brousseau, P.A., McGuire, K.J., Ross, D.S., 2014. Influence of landscape position and transient water table on soil development and carbon distribution in a steep, headwater catchment. Geoderma 226–227, 279–289.

Barcellos, D., Cyle, K.T., Thompson, A., 2018. Faster redox fluctuations can lead to higher iron reduction rates in humid forest soils. Biogeochemistry 137, 367–378.

Basile-Doelsch, I., Amundson, R., Stone, W.E.E., Borschneck, D., Bottero, J.Y., Moustier, S., Masin, F., Colin, F., 2007. Mineral control of carbon pools in a volcanic soil horizon. Geoderma 137 (3–4), 477–489.

Berry, A.J., O'Neill, H., St, C., Jayasuriya, K.D., Campbell, S.J., Foran, G.J., 2003. XANES calibrations for the oxidation state of iron in silicate glass. Am. Mineral. 88 (7), 967–977.

Bhattacharyya, A., Schmidt, M.P., Stavitski, E., Martínez, C.E., 2018. Iron speciation in peats: chemical and spectroscopic evidence for the co-occurrence of ferric and ferrous iron in organic complexes and mineral precipitates. Org. Geochem. 115, 124–137.

Black, C., Evals, D., White, J., Ensminger, L., Clark, F., 1965. Methods of Soil Analysis Part 1: Physical and Mineralogical Properties, Including Statistics of Measurement and Sampling. American Society of Agronomy, Madison, WI.

Bourgault, R.R., Ross, D.S., Bailey, S.W., 2015. Chemical and morphological distinctions between vertical and lateral podzolization at Hubbard Brook. Soil Sci. Soc. Am. J. 79 (2), 428–439.

Bourgault, R.R., Ross, D.S., Bailey, S.W., Bullen, T.D., McGuire, K.J., Gannon, J.P., 2017. Redistribution of soil metals and organic carbon via lateral flowpaths at the catchment scale in a glaciated upland setting. Geoderma 307, 238–252.

Breiman, L., 2001. Random forests. Mach. Learn. 45 (1), 5–32.

Buettner, S.W., Kramer, M.G., Chadwick, O.A., Thompson, A., 2014. Mobilization of colloidal carbon during iron reduction in basaltic soils. Geoderma 221–222, 139–145.

Chen, C., Dynes, J.J., Wang, J., Sparks, D.L., 2014. Properties of Fe-organic matter associations via coprecipitation versus adsorption. Environ. Sci. Technol. 48, 13751–13759.

Chen, K., Chen, T., Chan, Y., Cheng, C., Tzou, Y., Liu, Y., Teah, H., 2016. Stabilization of natural organic matter by short-range-order iron hydroxides. Environ. Sci. Technol. 50, 12612–12620.

Chen, C., Meile, C., Wilmoth, J., Barcellos, D., Thompson, A., 2018. Influence of pO2 on iron redox cycling and anaerobic organic carbon mineralization in a humid tropical forest soil. Environ. Sci. Technol. 52 (14), 7709–7719.

Chen, C., Thompson, A., 2018. Ferrous iron oxidation under varying pO2 levels: the effect of Fe(III)/Al(III) oxide minerals and organic matter. Environ. Sci. Technol. 52 (2), 597–606.

Chow, A.T., Tanji, K.K., Gao, S., Dahlgren, R.A., 2006. Temperature, water content, and wet-dry cycle effects on DOC production and carbon mineralization in agricultural peat soils. Soil Biol. Biochem. 38, 477–488.

Christensen, J.H., Krishna Kumar, K., Aldrian, E., An, S.-I, Cavalcanti, I.F.A., de Castro, M., Dong, W., Goswami, P., Hall, A., Kanyanga, J.K., Kitoh, A., Kossin, J., Lau, N-C., Renwick, J., Stephenson, D.B., Xie, S.-P, Zhou, T., 2013. Climate phenomena and their relevance for future regional climate change. In: Stocker, T.F., Qin, D., Plattner, G.-K., Tignor, M., Allen, S.K., Boschung, J., Nauels, A., Xia, Y., Bex, V., Midgley, P.M. (Eds.), Climate Change 2013: The Physical Science Basis. Contribution of Working Group I to the Fifth Assessment Report of the Intergovernmental Panel on Climate Change, Cambridge University Press, Cambridge, United Kingdom and New York, NY, pp. 1217–1308.

Coward, E.K., Thompson, A.T., Plainte, A.F., 2017. Iron-mediated mineralogical control of organic matter accumulation in tropical soils. Geoderma 306 (15), 206–216.

Coward, E.K., Thompson, A.T., Plainte, A.F., 2018. Contrasting Fe speciation in two humid forest soils: Insight into organomineral associations in redox-active environments. Geochim. Cosmochim. Acta 238, 68–84.

Das, S., Richards, B.K., Hanley, K.L., Krounbi, L., Walter, M.F., Walter, M.T., Steenhuis, T.S., Lehmann, J., 2019. Lower mineralizability of soil carbon with higher legacy soil moisture. Soil Biol. Biochem. 130, 94–104.

DeCiucies, S., 2018. When less is more: priming of soil organic matter by pyrogenic carbon (M.S. thesis). Cornell University, Ithaca, NY. DOI: https://doi.org/10.7298/X4B856CF.

Degens, B.P., Sparling, G.P., 1995. Repeated wet-dry cycles do not accelerate the mineralization of organic C involved in the macro-aggregation of a sandy loam soil. Plant Soil 175 (2), 197–203.

Gannon, J., McGuire, K., Bailey, S., 2017. Lateral water flux in the unsaturated zone: a mechanism for the formation of spatial soil heterogeneity in a headwater catchment. Hydrol. Process. 31 (20), 3568–3579.

Gillin, C.P., Bailey, S.W., McGuire, K.J., Gannon, J.P., 2015. Mapping of hydropedologic spatial patterns in a steep headwater catchment. Soil Sci. Soc. Am. J. 79, 440–453.

Ginn, B., Meile, C., Wilmoth, J., Tang, Y., Thompson, A., 2017. Rapid iron reduction rates are stimulated by high-amplitude redox fluctuations in a tropical forest soil. Environ. Sci. Technol. 51 (6), 3250–3259.

Gormanns, P., Reckow, S., Poczatek, C.J., Turck, C.W., Lechene, C., 2012. Segmentation of multi-isotope mass spectrometry data for semi-automatic detection of regions of interest. PLoS One 7 (2), e30576.

Hall, S.J., Liptzin, D., Buss, H.L., DeAngelis, K., Silver, W.L., 2016. Drivers and patterns of iron redox cycling from surface to bedrock in a deep tropical forest soil: a new conceptual model. Biogeochemistry 130 (1–2), 177–190.

Hall, S.J., Berhe, A.A., Thompson, A., 2018. Order from disorder: do organic matter composition and turnover co-vary with iron phase crystallinity? Biogeochemistry 140, 93–110.

Heckman, K., Lawrence, C.R., Harden, J.W., 2018. A sequential selective dissolution method to quantify storage and stability of organic carbon associated with Al and Fe hydroxide phases. Geoderma 312, 24–35.

Herndon, E., AlBashaireh, A., Singer, D., Chowdhury, T.R., Gu, B., Graham, D., 2017. Influence of iron redox cycling on organo-mineral associations in Arctic tundra soil. Geochim. Cosmochim. Acta 207, 210–231.

Huang, W., Hall, S.J., 2017. Optimized high-throughput methods for quantifying iron biogeochemical dynamics in soil. Geoderma 306, 67–72.

Inagaki, T.M., Possinger, A.R., Grant, K.E., Schweizer, S.A., Mueller, C.W., Derry, L.A., Lehmann, J., Kögel-Knabner, I., 2020. Subsoil organo-mineral associations under contrasting climate conditions. Geochim. Cosmochim. Acta 270, 244–263.

Jankowski, M., 2014. The evidence of lateral podzolization in sandy soils of Northern Poland. Catena 112, 139–147.

Jones, M.E., Nico, P.S., Ying, S., Regier, T., Thieme, J., Keiluweit, M., 2018. Manganese-driven carbon oxidation at oxic-anoxic interfaces. Environ. Sci. Technol. 52, 12349–12367.

Kalbitz, K., Kaiser, K., 2008. Contribution of dissolved organic matter to carbon storage in

forest mineral soils. J. Plant. Nutr. Soil Sci. 171, 52–60.
Kalbitz, K., Schmerwitz, J., Schwesig, D., Matzner, E., 2003. Biodegradation of soil-derived dissolved organic matter as related to its properties. Geoderma 133, 273–292.
Kayranli, B., Scholz, M., Mustafa, A., Hedmark, A., 2010. Carbon storage and fluxes within freshwater wetlands: a critical review. Wetlands 30 (1), 111–124.
Keiluweit, M., Wanzek, T., Kleber, M., Nico, P., Fendorf, S., 2017. Anaerobic microsites have an unaccounted role in soil carbon stabilization. Nat. Commun. 8 (1771).
Kleber, M., Eusterhues, K., Keiluweit, M., Mikutta, C., Mikutta, R., Nico, P.S., 2015. Mineral-organic associations: formation, properties, and relevance in soil environments. Adv. Agron. 130, 1–140.
Knicker, H., Lüdemann, H.D., 1995. N-15 and C-13 CPMAS and solution NMR studies of N-15 enriched plant material during 600 days of microbial degradation. Org. Geochem. 23, 329–341.
Kramer, M.G., Sanderman, J., Chadwick, O.A., Chorover, J., Vitousek, P.M., 2012. Long-term carbon storage through retention of dissolved aromatic acids by reactive particles in soil. Global Change Biol. 18 (8), 2594–2605.
Krounbi, L., van Es, H., Karanja, N., Lehmann, J., 2018. Nitrogen and phosphorus availability of biologically and thermochemically decomposed human wastes and urine in soils with different texture and pH. Soil Sci. 183 (2), 51–65.
Kuhn, M., 2008. Building predictive models in R using the “caret” package. J. Stat. Soft. 28 (5), 1–26.
Kurtz, A.C., Derry, L.A., Chadwick, O.A., Alfano, M.J., 2000. Refractory element mobility in volcanic soils. Geology 28 (8), 683–686.
Lehmann, J., Kleber, M., 2015. The contentious nature of soil organic matter. Nature 528, 60–68.
Lengke, M.F., Ravel, B., Fleet, M.E., Wanger, G., Gordon, R.A., Southam, G., 2006. Mechanisms of gold bioaccumulation by filamentous cyanobacteria from gold(III)-chloride complex. Environ. Sci. Technol. 40 (20), 6304–6309.
Lundquist, E.J., Jackson, L.E., Scow, K.M., 1999. Wet-dry cycles affect dissolved organic carbon in two California agricultural soils. Soil Biol. Biochem. 31, 1031–1038.
Mayer, S., Schwindt, D., Steffens, M., Völkel, J., Kögel-Knabner, I., 2018. Drivers of organic carbon allocation in a temperate slope-floodplain catena under agricultural use. Geoderma 327, 63–72.
McGuire, K., Bailey, S.W., Gannon, J.P., 2016. Water level recordings from wells in Watershed 3 at the Hubbard Brook Experimental Forest, 2007 - present. Environ. Data Initiative. https://doi.org/10.6073/pasta/a7b6b61df98b65244eba64d8bc391582. Dataset accessed 1/26/2020.
Parfitt, R.L., Childs, C.W., 1988. Estimation of forms of Fe and Al – a review, and analysis of contrasting soils by dissolution and Mossbauer methods. Aust. J. Soil Res. 26 (1), 121–144.
Petrone, K.C., Richards, J.S., Grierson, P.R., 2009. Bioavailability and composition of dissolved organic carbon and nitrogen in a near coastal catchment of south-western Australia. Biogeochem. 92 (1–2), 27–40.
Preston, C.M., Dudley, R.L., Fyfe, C.A., Mathur, S.P., 1984. Effects of variations in contact times and copper contents in a $^{13}$C CPMAS NMR study of samples of four organic soils. Geoderma 33, 245–253.
Prietzel, J., Thieme, J., Eusterhues, K., Eichert, D., 2007. Iron speciation in soils and soil aggregates by synchrotron-based X-ray microspectroscopy (XANES, μ-XANES). Eur. J. Soil Sci. 58, 1027–1041.
Rasmussen, C., Heckman, K., Wieder, W.R., Keiluweit, M., Lawrence, C.R., Berhe, A.A., Blankinship, J.C., Crow, S.E., Druhan, J.L., Hicks Pries, C.E., Marin-Spiotta, E., Plante, A.F., Schädel, C., Schimel, J.P., Sierra, C.A., Thompson, A., Wagai, R., 2018. Beyond clay: towards an improved set of variables for predicting soil organic matter content. Biogeochemistry. 137, 297–306.
Ravel, B., Newville, M., 2005. Athena, Artemis, Hephaestus: data analysis for X-ray absorption spectroscopy using IFEFFIT. J. Synchrotron Rad. 12, 537–541.
Core Team, R., 2017. R: A language and environment for statistical computing. R Foundation for Statistical Computing, Vienna, Austria.
Ross, G.J., Wang, C., 1993. Extractable Al, Fe, Mn, and Si. In: Carter, M.R (Ed.), Soil Sampling and Methods of Analysis. Canadian Society of Soil Science, Lewis Publishers, Boca Raton, pp. 239–246.
Scheel, T., Dörfler, C., Kalbitz, K., 2007. Precipitation of dissolved organic matter stabilizes carbon in acidic forest soils. Soil Sci. Soc. Am. J. 71, 64–74.
Schöning, I., Knicker, H., Kögel-Knabner, I., 2005. Intimate association between O, N-alkyl carbon and iron oxides in clay fractions of forest soils. Org. Geochem. 36, 1378–1390.
Schmidt, M.W., Torn, M.S., Abiven, S., Dittmar, T., Guggenberger, G., Janssens, I.A., Kleber, M., Kögel-Knabner, I., Lehmann, J., Manning, D.A.C., Nannipieri, P., Rasse, D.P., Weiner, S., Trumbore, S.E., 2011. Persistence of soil organic matter as an ecosystem property. Nature 478 (7367), 49–56.
Schneider, C.A., Rasband, W.S., Eliceiri, K.W., 2012. NIH Image to ImageJ: 25 years of image analysis. Nat. Methods 9 (7), 671–675.
Shang, C., Zelazny, L.W., 2008. Selective dissolution techniques for mineral analysis of soils and sediments. In: Ulery, A.L., Drees, L.R. (Eds.), Methods of Soil Analysis, Part 5, Mineralogical Methods. SSSA Book Series No. 5. Soil Science Society of America, Madison, WI, pp. 33–80.
Silver, W.L., Lugo, A.E., Keller, M., 1999. Soil oxygen availability and biogeochemistry along rainfall and topographic gradients in upland wet tropical forest soils. Biogeochemistry 44 (3), 301–328.
Six, J., Conant, R.T., Paul, E.A., Paustian, K., 2002. Stabilization mechanisms of soil organic matter: implications for C-saturation of soils. Plant Soil 241 (2), 155–176.
Sommer, M., Halm, D., Weller, U., Zarei, M., Stahr, K., 2000. Lateral podzolization in a granite landscape. Soil Sci. Soc. Am. J. 64 (4), 1434–1442.
Sutfin, N.A., Wohl, E.E., Dwire, K.A., 2016. Banking carbon: a review of organic carbon storage and physical factors influencing retention in floodplains and riparian ecosystems. Earth Surf. Process. Landf. 41 (1), 38–60.
Thompson, A., Chadwick, O.A., Boman, S., Chorovor, J., 2006a. Colloid mobilization during soil iron redox oscillations. Environ. Sci. Technol. 40 (18), 5743–5749.
Thompson, A., Chadwick, O.A., Rancourt, D.G., Chorovor, J., 2006b. Iron-oxide crystallinity increases during soil redox oscillations. Geochim. Cosmochim. Acta 70 (7), 1710–1727.
Thompson, A., Rancourt, D.G., Chadwick, O.A., Chorovor, J., 2011. Iron solid-phase differentiation along a redox gradient in basaltic soils. Geochim. Cosmochim. Acta 75 (1), 119–133.
Torn, M.S., Swanston, C.W., Castanha, C., Trumbore, S.E., 2009. Storage and turnover of organic matter in soil. In: Senesi, N., Xing, B., Huang, P.M. (Eds.), Biophysico-Chemical Processes Involving Natural Nonliving Organic Matter in Environmental Systems. John Wiley & Sons Inc, Hoboken, NJ, pp. 219–272.
Ussiri, D.A.N., Johnson, C.E., 2004. Sorption of organic carbon fractions by Spodosol mineral horizons. Soil Sci. Soc. Am. J. 68, 253–262.
Vermeire, M.-L., Bonneville, S., Stenuit, B., Delvaux, B., Cornélis, J.-T., 2019. Is microbial reduction of Fe (III) in podzolic soils influencing C release? Geoderma 340, 1–10.
Viollier, E., Inglett, P.W., Hunter, K., Roychoudhury, A.N., Van Cappellen, P., 2000. The ferrozine method revisited: Fe(II)/Fe(III) determination in natural waters. Appl. Geochem. 15, 785–790.
Vogel, C., Mueller, C.W., Höschen, C., Buegger, F., Katja, H., Shulz, S., Schloter, M., Kögel-Knabner,, 2014. Submicron structures provide preferential spots for carbon and nitrogen sequestration in soils. Nat. Commun. 5, 2947. https://doi.org/10.1038/ncomms3947.
Wieder, W.R., Cleveland, C.C., Townsend, A.R., 2008. Tropical tree species composition affects the oxidation of dissolved organic matter from litter. Biogeochemistry 88 (2), 127–138.
Whitman, T., Zhu, Z., Lehmann, J., 2014. Carbon mineralizability determines interactive effects on mineralization of pyrogenic organic matter and soil organic carbon. Environ. Sci. Technol. 48 (23), 13727–13734.
Winkler, P., Kaiser, K., Thompson, A., Kalbitz, K., Fiedler, S., Jahn, R., 2018. Contrasting evolution of iron phase composition in soils exposed to redox fluctuations. Geochim. Cosmochim. Acta 235, 89–102.
Yang, W.H., Liptzin, D., 2015. High potential for iron reduction in upland soils. Ecology 96 (7), 2015–2020.
Zhao, Q., Poulson, S.R., Obrist, D., Sumaila, S., Dynes, J.J., McBeth, J.M., Yang, Y., 2016. Iron-bound organic carbon in forest soils: quantification and characterization. Biogeosciences 13, 4777–4788.